The 8th International Supercritical CO_2 Power Cycles Symposium
February 27 – 29, 2024, San Antonio, Texas
Paper 114

Technical feasibility analysis and thermo-mechanical modelling of a high temperature solar receiver and a shell and tube heat exchanger for next generation CSP plants

Sara Pace[1], Pablo Rodríguez-deArriba[2], Francesco Crespi[2], Giampaolo Manzolini[1], David Sánchez[2]

[1]Politecnico di Milano (Italy), [2]University of Seville (Spain)

Sara Pace obtained a MSc. in Energy Engineering at Politecnico di Milano, developing her MSc. thesis during a reasearch period at University of Seville, under the joint supervision of Prof. Giampaolo Manzolini and Prof. David Sánchez. Her main area of interest includes renewable energy power generation systems, in particular CSP and wind. She has recently started working as Junior Offshore Wind Asset Coordinator at Plenitude.

Pablo Rodríguez de Arriba is a Ph.D. Student in Energy Engineering at the University of Seville. His thesis is focused on the techno-economic optimisation and integration of innovative CO_2-based technology for Concentrated Solar Power applications, within the framework of the SCARABEUS project. His areas of interest also include thermodynamics, heat transfer, non-conventional working fluids, renewable energies, desalination, WHR and refrigeration.

Francesco Crespi is a lecturer in Fluid Mechanics at the University of Seville, where he currently works at the Department of Energy as a postdoctoral fellow. Mr. Crespi started his research activity at the beginning of 2015 after completing a Double Degree project in Industrial Engineering between University of Seville and Politecnico of Milan. His research activity is focused on numerical simulation of sCO_2 power cycles and analysis of possible dopant candidates for CO_2 blends.

Giampaolo Manzolini is a Full Professor in Energy Systems and Power generation at Politecnico di Milano, where he currently works at the Department of Engineering. His main research activity focuses on CSP systems and supercritical CO_2 power cycles. In this regard, he is the coordinator of two H2020 EU-funded project, namely Scarabeus and Desolination. He is also the promoter and co-responsible of $SolarTech^{LAB}$ and the Laboratory of Microgrids at Politecnico di Milano.

David Sánchez is a Full Professor in Energy Systems and Fluid Machinery at the University of Seville. He has fifteen years' experience in the field of stationary power generation using turbomachinery in combination with novel cycle concepts that can introduce step-changes in the Concentrated Solar Power industry, thus enabling higher efficiencies and lower electricity costs. He has conducted research to integrate the sCO_2 power cycle into CSP and WHR applications for more than ten years, both with private and public funding at the fundamental and applied levels.

Abstract

As the pursuit of lower LCOE intensifies for concentrated solar power (CSP) plants, the need for exploring new technologies becomes more pressing. This study focuses on the design of two key components of a CSP plant: the solar receiver and the particle-to-sCO_2heat exchanger. A literature review of high-temperature receivers has been conducted and free-falling particle receivers (FFPRs) have been identified as a promising technology for next-generation CSP plants. A FFPRs model from literature has been implemented and validated. In particular, the study aims to optimize the heat exchanger's performance by implementing a particle heat transfer coefficient model, which has not been thoroughly evaluated and fully presented in existing literature. Furthermore, the study analyzes and compares s$CO_2$with a new fluid mixture to achieve higher performances, evaluated through the overall heat transfer coefficient, and compactness of the heat exchanger. With the aid of simulation tools and computational models, the proposed design strategies offer a promising pathway for achieving the ambitious LCOE target, reducing the heat exchanger dimension and optimizing the efficiency of the solar tower, evaluating a three-receiver configuration. The study places a particular emphasis on the particle-to-sCO_2heat exchanger, which is a critical component for achieving higher efficiency and lower costs in CSP power plants. The novel design approach and the incorporation of the heat transfer coefficient in the model could significantly improve the performance of the heat exchanger coupled with a free-falling particle receiver and drive the CSP technology to new heights. Overall, this work represents a first step towards developing sustainable and cost-effective energy solutions by improving the design of CSP power plants.

1 Introduction

The increasing demand for energy and the growing concern over climate change have led to a focus on renewable energy sources, such as solar power [1]. Solar power has become one of the most rapidly growing renewable energy sources, with concentrated solar power (CSP) being one of the most promising technologies for achieving sustainable energy generation [1]. CSP uses mirrors or lenses to concentrate the sun's rays onto a small area, which heats up a fluid, typically a molten salt or water, to generate steam. The steam is then used to power turbines which, in turn, generate electricity. One of the critical components of a CSP system is the solar receiver, which absorbs and converts the concentrated solar energy into heat. There are two main types of solar receivers: low-temperature receivers (LTRs) and high-temperature receivers (HTRs). LTRs are designed to operate at temperatures up to 600°C, while HTRs can even operate at temperatures above 800°C. HTRs are essential for achieving higher thermal efficiency and reducing the cost of electricity generation in CSP systems, becoming competitive on the electricity market [2].

In recent years, there has been a significant focus on the development of high-temperature receivers [2]. This is because HTRs enable the use of higher temperature fluids, such as supercritical carbon dioxide (sCO_2), which has excellent thermodynamic properties and can lead to a significant increase in the efficiency of the system [2]. sCO_2 is an ideal fluid for use in CSP systems due to its high thermal conductivity, low viscosity, and non-flammability. The use of sCO_2 also requires the development of new heat exchanger technologies, specifically particle to sCO_2 heat exchangers, which are designed to transfer heat from the particles to the sCO_2 fluid. These heat exchangers are critical components of the CSP system, as they play a significant role achieving high thermal efficiency and reducing the cost of electricity generation. [3]. These components are essential for achieving high thermal efficiency and reducing the cost of electricity generation in CSP systems. The development of these technologies is crucial for the continued growth of CSP,

and lately there has been a significant focus on research and development in these areas.

CSP has several advantages over other renewable energy sources, such as wind and solar photovoltaic (PV) systems. One of the most significant is its ability to store energy, allowing for the generation of electricity during periods when the sun is not shining [4, 5]. This is achieved through the use of thermal energy storage (TES) systems, which store the heat generated during the day and release it at night when the demand for electricity is higher. Another advantage of CSP is its ability to provide dispatchable power, which means that the system can be turned on and off based on the demand for electricity. This is in contrast to wind and solar PV systems, which are dependent on weather conditions and cannot be turned on or off at will. CSP also has the potential to provide electricity to remote areas that are not connected to the power grid. This is because CSP systems can be designed to operate independently and do not require a connection to the power grid. This is especially important for developing countries, where many people do not have access to electricity.

In addition to what mentioned above, CSP could reduce greenhouse gas emissions and mitigate climate change. According to a report by the International Energy Agency (IEA), CSP has the potential to generate 11% of the world's electricity by 2050 and reduce greenhouse gas emissions by 4 billion tons per year [6].

Bearing this in mind, the aim of this paper is to model the solar subsystem of a next-generation CSP plant combined with sCO_2 power cycles. The manuscript starts with a comprehensive literature review to identify the optimal solar receiver configuration. The focus is primarily on comparing centrifugal and falling particle receivers, but alternative technologies (volumetric receivers, molten salts receivers) are also taken into account. Once the technology of interest is selected (falling particle receiver), it is modelled and validated using reference models from Gonzáles-Portillo [7]. The second part of the manuscript involves a review of particle heat exchangers to choose the best model to complement the falling particle receiver. The selected model, among particle-to-sCO_2 HX, is the shell and tube heat exchanger, which is modelled by integrating the heat transfer coefficient calculation on the particle side. The model is then validated against the COMPASsCO_2S heat exchanger model. Additionally, the design is examined with different fluids for further investigation.

2 Literature review of solar tower receivers

Solar receivers are critical components in concentrated solar power (CSP) plants, particularly in Solar Power Tower plants [1, 2], as they allow to convert the concentrated solar radiation into useful thermal energy, which can be ultimately converted into electricity through a power cycle. They highlight the high efficiency of high-temperature central tower plants, which can reach up to 50%, as well as their potential for integration with other renewable energy sources and with thermal energy storage systems to provide energy even with lacking solar radiation. Future research aims to develop and design more efficient receivers capable of withstanding high temperatures in terms of both materials and performance [1, 8].
Over the years, many receiver configurations have been proposed, although only a few have been commercialized. The available models have been classified according to various criteria. Firstly, receivers are divided into two types: external receivers, where the incident solar radiation strikes the outer surface, and cavity receivers, where the solar radiation is concentrated in a cavity through a window. Cavity receivers have been deemed the most suitable model for achieving high temperatures due to their high absorption, which reduces overall losses, although this is considered one of the main goals for the future. Receivers can also be categorized based on the type of heat transfer fluid (HTF) into gas, liquid, or solid particle receivers [9].

2.1 Gas Receivers

Subcategories of gas receivers include volumetric, tubular, and small particles air receivers [2].

2.1.1 Volumetric Receivers

Volumetric receivers, shown in Fig.[1], can be classified based on factors such as potential power plant configuration (open or closed systems), geometry, material, and power output [2]. The configurations can be either atmospheric or pressurized receivers.

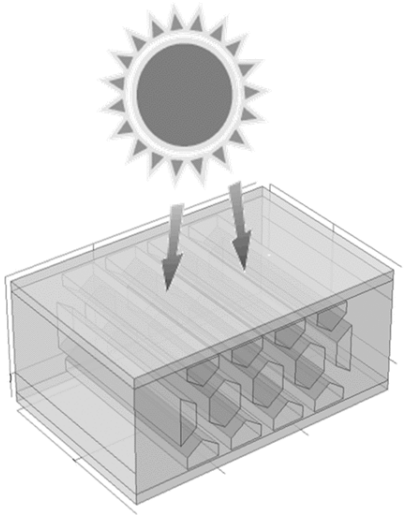

Figure 1: *Volumetric receiver. [10]*

In atmospheric receiver systems, a blower forces a stream of air through the absorber material, causing the air temperature to rise. Waste heat recovery boilers downstream of the receiver are

usually present in open loop configurations, and are responsible for the steam generation that drives the steam turbine in the power block [2].

Pressurized receiver systems are the most common in gas turbine applications. Receivers are installed downstream of the compressor to increase the temperature of the compressed air. Both closed loop and open loop configurations are possible, with the former consisting of a volumetric receiver receiving pressurized air at low temperature and sending it to either a supplementary combustor or the turbine directly. The lower the temperature gap between receiver outlet and turbine inlet, the lower the carbon footprint of the electricity produced [2].

Volumetric receivers can be made of different materials, such as metals and ceramics. Stainless steel, Incoloy, and alloy are considered the main options for absorbers. Ceramics have also been used because they can withstand higher temperatures, up to 1200°C, compared to metals [2]. Studies have shown that the efficiency of volumetric receivers is influenced by several factors, such as the shape and size of the receiver, the type of absorber material used, and the flow rate and temperature of the working fluid. Some studies have explored the use of multi-tube receivers to increase the surface area available for heat transfer [11].

2.1.2 Tubular Receivers

Gas tubular receivers can be categorized based on the type of loop they are configured with - open or closed loop - which is dependent on the design pressure of the heat transfer fluid (HTF). In an open loop system, the HTF is exposed to the environment and is not recycled, while in a closed loop system, the HTF is enclosed within a piping system and is continuously recycled. Another interesting configuration of gas tubular receivers involves the use of dense particles that are suspended in a gas flow stream. Thus, the particles are of small dimensions and can be easily fluidized at low velocities. This approach can potentially increase the efficiency of the system by providing more surface area for heat transfer [2]. Several studies have investigated the use of particles in gas receivers. Here in Ref.[12], the authors evaluated the performance of a gas-solid receiver that used dense ceramic particles as the heat transfer medium.

2.2 Liquid Receivers

In certain receiver configurations, the Heat Transfer Fluid (HTF) is in liquid phase, and it could even be regular water. One of the significant environmental advantages of using water as the HTF is the almost zero impact of having leakages in the entire system or using it directly for both HTF and working fluid in the power block, as long as the configuration includes a Rankine cycle. However, liquid receivers have some disadvantages, such as the maximum heat flux that these receivers' configurations can withstand, which is typically in the range of 200-500 $\frac{kW}{m^2}$, and lower thermal capacity when compared to molten salts or sodium [13].

2.2.1 Tubular Liquid Receivers

The most exploited HTF among liquid tubular receivers in concentrated solar power plants is either molten salts [see Fig.2] or sodium [14]. In tubular receivers involving molten salts, a fraction of the flow is sent to the steam generator heat exchanger, while the remaining flow is sent to a hot insulated tank for storage. When needed, these hot salts are retrieved and used to generate steam, which drives the steam turbine and produces mechanical power. Another clear advantage of using molten salts is the higher heat flux admissible on the solar receiver surface. This is due to the higher capacity of the fluid flowing inside, which enables a higher concentration factor and higher efficiencies on the receiver side. This, in turn, impacts the overall efficiency of the

power plant as well [15]. However, molten salts configurations have some limitations, such as decomposition and solidification of the fluid, which narrow the range of operating temperatures from 250°C to 600°C. Receiver efficiencies range from 84% to 89% [16]. In addition to molten salts as HTF, liquid sodium is being also investigated as it has several advantages due to its high boiling point (883°C) and high thermal conductivity [17, 18]. However, liquid sodium is also highly reactive with water and air, which can lead to safety concerns. Sodium reacts violently with water, producing hydrogen gas and heat, which can lead to explosions. Additionally, liquid sodium can ignite on contact with air, which can lead to fires. For these reasons, special precautions must be taken when handling and storing liquid sodium in CSP systems [19]. Molten salts or sodium are not the only HTF exploited for CSP power plants, although they are considered the state of the art of solar tower CSP power plants. Investigations over the use of metal as the HTF have also been carried out. Using metal as the HTF has some important advantages, such as thermal stability and very high saturation temperature, although the low specific heat capacity prevents it from being used as a heat storage medium [20].
Among high-temperature receivers, molten glass is being investigated as an alternative to molten salts as an HTF. Glass acts as an effective volumetric absorber of solar radiation and is able to withstand high temperatures over 1000°C. In the case of clear glass, it was not possible to increase the melting temperature without overheating the bottom of the crucible, with the maximum temperature achieved being 1145°C. The resulting melt was considered quite heterogeneous as most of the air loaded with glass got trapped in the melt due to the high viscosity of the mixture, especially near the crucible walls. However, with other colors of glass, higher temperatures of up to 1300°C have been reached and maintained for at least 5 hours, resulting in a more homogeneous melt with fewer trapped air bubbles [21].

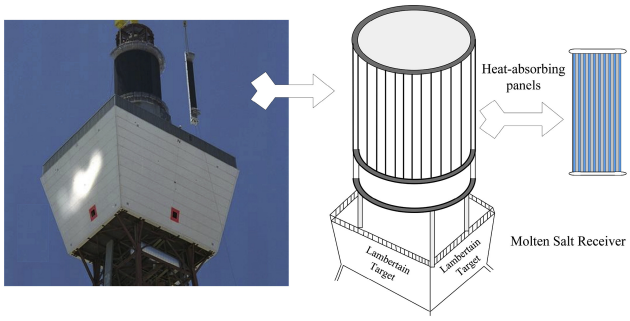

Figure 2: *Molten salts receiver. [22]*

2.2.2 Falling Film Receivers

Falling film receivers are based on gravity-driven fluid motion: the HTF in liquid phase flows down an inclined wall whilst being directly or indirectly hit by solar radiation. Consequently, two main types of receivers can be defined depending whether the fluid is heated by solar radiation or by an illuminated surface.

2.3 Solid Particle Receivers

The solid particle receiver technology involves the use of sand-like ceramic particles that fall across the receiver in a particle curtain, while the cavity of the receiver is irradiated by the solar flux. The particles are heated through an energy absorption process, and the technology enables easier implementation of thermal energy storage (TES) and easy scaling-up [2]. The residence time is a

crucial parameter in the solid particle receiver model, which can be increased by recirculating the particles, although this may lead to problems related to the particle elevator. Wind direction can also affect the efficiency of the receiver. The efficiency of the receiver model is expected to reach 80%, and crucial parameters for higher efficiencies include particles, aero-window air jet flow, and residence time. Heat exchanger design and particle conveyance technologies are reported to be major concerns [2]. The materials used for the proppants include silica, alumina, zircon, and iron-doped Al_2O_3 particles. Further classification has been made according to the particle-cavity arrangement.

2.3.1 Obstructing Particle Receiver

Porous materials or an array of obstacles can be used to obstruct the flow of particles in obstructing solar particle receiver [see Fig.3] and increase their residence time in the irradiated curtain [23]. However, the effectiveness of these approaches is still under investigation due to the high temperatures and particle heat capacity, which can cause oxidation of the porous materials. Recent research [24, 25] has highlighted this issue.

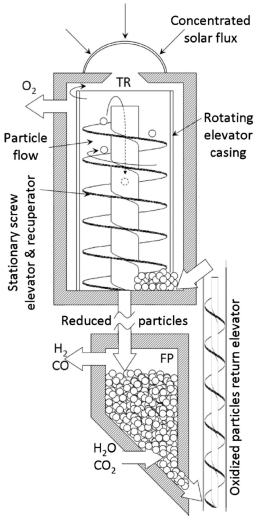

Figure 3: *Obstructing particle receiver. [2]*

2.3.2 Fluidized Particle Receivers

The indirect particle receiver configuration uses a fluidized bed of particles to transfer heat from concentrated solar irradiation to the working fluid. In this configuration, particles are forced upward through tubes by airflow, and the tubes are irradiated by solar energy [see Fig.4] [26]. The fluidization of the particles by the airflow increases the overall heat transfer process [27], leading to high suspension temperatures at the outlet of the irradiated tubes of up to 750°C . However, a major challenge in this configuration is the parasitic energy required to fluidize the particle flow inside the tubes. Researchers have investigated different design and operational parameters to optimize the system's performance, such as particle size, fluidization velocity, and tube geometry [28].

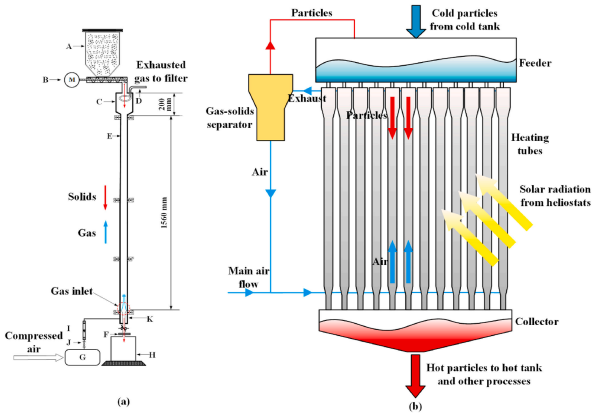

Figure 4: *Fluidized particle receiver. [29]*

2.3.3 Gravity Driven Particle Flow Receivers

The particles in this configuration are forced downward by gravity to flow through an enclosure characterized by a staggered array of tubes, as shown in Fig. [5]. This model is part of indirectly heated particle receivers [11, 30], and has been proposed between 2013 and 2015. Tubes are here irradiated by concentrated light on the interior surfaces while transferring heat to the particles flowing around the exterior side. Small-scale tests and models were performed and showed that the heat transfer to the particles was limited in locations around the tubular structures where the particles lost contact with the heated wall surfaces [30].

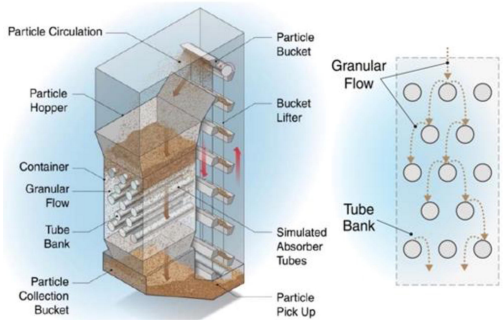

Figure 5: *Gravity driven particle receiver scheme. [2]*

2.3.4 Centrifugal Receivers

This receiver model, called CentRec [see Fig.7], was patented in the 2010s by DLR researchers [31–34],and has been tested in a solar simulator in Germany, with recent tests scaled up to 300 kW [see Fig.6] [35]. The CentRec receiver operates by inserting particles into a rotating drum via a feeding cone, where they are accelerated to a specific degree, allowing the centrifugal force to overcome the gravitational force and form a particle film on the cavity walls. The rotation axis is inclined to partially counteract the gravity force in the axial direction. By regulating the rotational speed, particle residence time, and film thickness on the wall, high heat flux and temperatures above 1000°C can be achieved. The design of the receiver reduces convection losses due to the inclination of the receiver case and the small aperture on the front, which also reduces radiation and particle losses. Efficiencies are expected to reach up to 90% [35]. However, the CentRec

receiver design also has some drawbacks, such as parasitic losses due to the constant circular case movement and the complexity of the design, which require computational fluid dynamics (CFD) modeling [36–38].

Figure 6: *Real centrifugal experimental receiver by DLR. [38]*

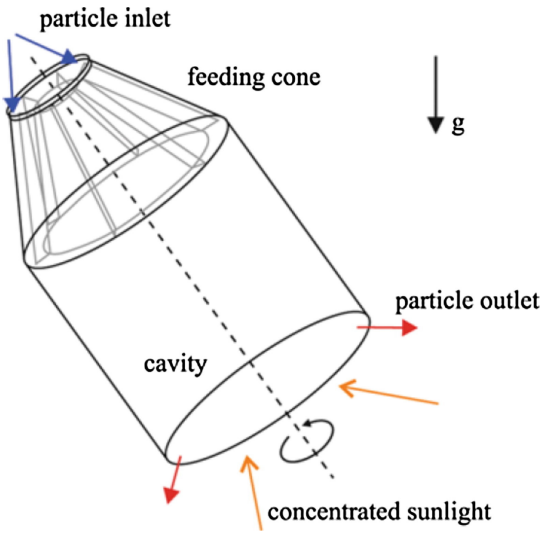

Figure 7: *Centrifugal receiver scheme. [2]*

2.3.5 Free Falling Particle Receivers

The mechanism of free falling particle receivers (FSPR) is a simple and widely used technology in concentrated solar power plants, and also coupled with hydrogen production [39], due to its direct absorption of solar irradiation on a curtain of solid particles. The FSPR coupled with a thermal energy storage system has been under investigation since the early 80s by Sandia National Laboratory [40, 41]. The FSPR-TES system configuration, as shown in Fig.[8], involves cold solid particles falling under gravity through the top of the receiver cavity. The particles are irradiated by concentrated sunlight entering through a window, thus absorbing solar radiation which can heat them up to 1000°C [8, 42]. The heated solid particles then exit the receiver cavity and are stored in an insulated hot storage tank. When required, the particles flow through a heat exchanger (HX), where the working fluid is heated, creating a power cycle. The solid particles serve as both heat transfer fluid and heat storage medium. The cooled solid particles are then stored in a cold storage tank and lifted back up to the top of the FSPR using a particle elevator, where the process is repeated [43]. Many investigations have been conducted on this receiver configuration, in order to define adequate heat transfer models [44]. Optimization on the efficiency has revealed that this technology is easy to scale up [45].

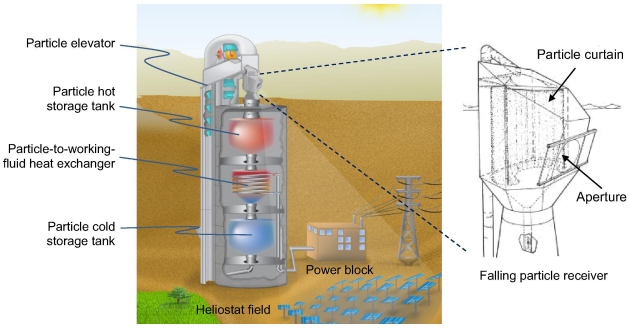

Figure 8: *Free falling particle receiver scheme. [46]*

3 Receiver Model

3.1 Selection of the configuration

The final choice on the configuration of the model fell eventually on the falling particle receiver one. Gas receiver, as stated in Sec.[2.1], cannot be coupled with TES systems, which are considered a mandatory feature in order to achieve goals such as using CSP in dispatchability systems and as storage of thermal energy when solar irradiation is not available. Liquid receivers, in particular molten salts receivers, are currently the state-of-the-art. However, in order to work with sCO_2 power cycles, high temperatures are required and molten salts suffer from degradation and efficiency loss for temperatures above 600°C. Further investigations are being held on new liquid HTF [47] and from the study LBE (Leas Bismuth) and Sodium seems to be the more promising, although its high flammability as explained in Sec.[2.2.1]. The main issue regarding the centrifugal receiver proposed by DLR and COMPASsCO_2 was the fact that most of the model included either CFD calculation or were too complex to be implemented. *"A centrifugal particle receiver for high-temperature solar applications, 2014"* (Ref.[36]), PhD thesis by Wei Wu proposed a simplified model in which no FEM (Finite Elements Method) analysis is involved for the particle motion forecast, which is computed as a compact fluid in the cavity moving in a helicoidal path. For the

calculation of the heat transfer model both ANSYS and CFD analysis have been involved. *"Modelling solar particle receivers with the Discrete Element Method, 2019"* (Ref.[38]), by Johannes Grobbel and *"Numerical Heat Transfer Modelling of a Centrifugal Solar Particle Receiver, 2022"*, by Hicdurmaz et al.(2022) (Ref.[37]), both proposed a DEM modelling for the particle motion, using a DEM open source called LIGGGHTS. Monte Carlo Ray Tracing was implemented as well in order to compute the incident heat flux, but since the model had been developed to follow each particle, it has been considered too computationally expensive to implement. Falling particle receiver, finally, seems to be the most suitable arrangement regarding this investigation and the goals and the possibility of this technology to be coupled with a TES system [48]. Particles are cheaper, as it is explained in Sec.[3.3] and widely available on the market, which makes also the cost related to the overall power plant lower. In addition, particles can stand really high temperatures, although they may suffer from ageing [49]. In addition, private communication with commercial partners (Abengoa Solar) confirmed the choice stating that, in the short-to-mid term, molten salts are not considered feasible from the technical point of view, due to the high temperatures targets to fulfil the LCOE goals. A final comparison between the two particles technologies has been carried out in Tab.[1].

Table 1: *Final comparison between the two most promising receivers: free falling particle and centrifugal receiver.*

Final Comparison		
	Falling Particle	**Centrifugal Receiver**
Residence Time	Low and to be optimized	Controlled by the rotational speed
High Temperatures	Achievable, up to 1000°C	Achievable, above 1000°C
Efficiency	Expected to reach 90%	Expected to reach 90%
Parasitic Losses	Relatively low for the particle lift, which is affected by low reliability due to the high temperatures	High because of the continuous rotation of the casing
Particles Layering	Curtain thickness varies along the vertical direction, along with the volume fraction of the particles	1-layer case wall covering assumed
Thermal Model Available	Both thermal and optical properties models are available, with no CFD analysis involved	Either the particle tracing or thermal model involve CFD analysis; extremely computationally expensive
Particle Motion Model	Pretty simple as the only force involved is gravity force in the vertical direction. Easy to model	Forecasting may not include CFD analysis, but most of the models follow each particle one by one

3.2 Modelling

The goal of this section is to describe the model of the receiver, required to have the final conclusion for the overall scope. The receiver model implemented was inspired by the one from L.F. González-Portillo, K. Albrecht, C.K. Ho [7]. although some simplifications have been taken into account. In their investigation, the main references of the research were the model from K. Albrecht and C.K. Ho, respectively Ref.[43, 50]. The differences implemented and added to the model in González-Portillo investigation regarded the heat loss model, indeed the calculation of convection and radiation losses were upgraded, as well as the calculation of the initial thickness needed in order to achieve a certain mass flow rate.
The receiver model follows the free falling particle receiver power plant configuration in Fig.[8], characterised by a power block with super-critical CO_2 as the working fluid (WF).

3.2.1 Hypothesis and input parameters

In order to model the receiver, boundary conditions have been defined and given by the University of Seville.
The receiver is characterised with a particle curtain, with both a front part and a back part exchanging heat, a back wall and the ambient. The window has been modelled as if the overall curtain is being irradiated through it, so the ratio between the curtain area and the window area will be equal to one. In reality, the ratio of the irradiated curtain area and the overall curtain area is 0.9, but this value will only affect the view factor in the radiative losses equation, in which $F = 0.9$ as estimated by González-Portillo [7]. The receiver is then modelled using a reduced order model: the important physics have been captured over the single vertical dimension, along the y-axis, which corresponds also to the falling direction of the particles.
The aspect ratio of the receiver has been considered equal to 1, as in the reference paper.

$$Aspect\ Ratio = \frac{Curtain\ Height}{Diameter\ of\ Receiver} = 1$$

The curtain is then assumed to be a square, which will lead to having a curtain width equal to the curtain height. The receiver has been discretizised: the overall vertical area of the curtain has been divided into N equal parts, which will be hit by the same irradiance value. The decision of the discretization has been carried out in order to have a more specific analysis, especially on the losses and on the computation of the temperature gradient along both the back wall and the falling particle curtain. Final input and design parameters are summarised in Tab.[2].

Table 2: *Design and operational parameters.*

Parameter	Value	Unit
Wall thickness, th_w	0.05	m
Back wall thickness, th_{bw}	0.05	m
Particle diameter, d_p	350	μm
Initial subdivision, N	40	-
Ambient temperature	35	°C
Outlet particle temperature	800	°C
Back wall conductivity, k_{bw}	0.2	$\frac{W}{m^2K}$
Back wall HTC, h_{bw}	10	$\frac{W}{m^2K}$
Back wall emissivity, ε_{bw}	0.8	-
Advection HTC h_{adv}	95	$\frac{W}{m^2K}$

3.3 Particles

In high temperatures free falling particle receiver applications, ceramic and silica particles have been investigated. The first ones are considered to be more suitable for direct-heating particle receivers, as they are characterised with high solar absorption properties and durability. These particles have also a low impact on the variable costs of CSP power plant and their relative LCOE, as they are considered to be very cheap. However, they lack high solar absorptance and they have showed some issues related to high temperatures withstand. Spherical sintered bauxite particles have instead a really high absorptance (α), higher than 90%, and they have proved to be very resistant to abrasion and chemical changes at high temperatures and pressures. The only drawback of sintered bauxite is the oxidation of the particle, which may reduce the thermal properties, included the absorptance: indeed, the continuous heating in the air for temperatures higher than 700°C and for over 500 hours affects the characteristic parameter α negatively due to the surface oxidation. A rejuvenating process through a thermal or chemical reduction is possible, in order to recover the loss on the absorption side. Ceramic are not affected by degradation and decreasing in the absorption parameter.

Among previous particle flow studies regarding solar receivers, it has been shown that the particle flow characteristics, such as velocity, curtain thickness, solids' volume fraction, and curtain opacity, are affected by the window area, the particle diameter and by external conditions (e.g., the wind [51]). In the paper reference reviewed during my investigation, the author, C.K. Ho, has used CARBO ID50 [see Tab. 3] [Ref. [43]] particles by CARBO. These particles have been proved to be very resistant at really high temperatures and to have excellent durability and good radiative properties.

The CARBO ID50 particles have been considered as the more suitable for my investigation, therefore they were implemented in the Matlab code, along with some reference particles that will be later used for the validation of the model [see Tab.4] [7]. It should be noted that Gonzales Portillo's Ref. [7] assumes a constant value for the particle's specific heat capacity coefficient. However, the model design presented in this paper takes into account that the specific heat capacity will vary with temperature, as the temperature difference across the particle curtain is not insignificant. Therefore, an adjustment is necessary to incorporate this variability in the model.

Table 3: *Carbo ID50 particles characteristics.*

Parameter	Value	Unit
Density, ρ_p	3300	$\frac{kg}{m^3}$
Thermal conductivity @1000 °C, k_p	2	$\frac{W}{mK}$
Specific heat capacity, c_p	$365 \cdot T^{0.18}$	$\frac{J}{kgK}$
Packed bed solar absorptance, α_p	0.91	-
Packed bed thermal emittance, ε_p	0.75	-

Table 4: *Reference particles characteristics.*

Parameter	Value	Unit
Density ρ_p	3550	$\frac{kg}{m^3}$
Thermal conductivity, k_p	2	$\frac{W}{mK}$
Specific heat capacity, c_p	1200	$\frac{J}{kgK}$
Packed bed solar absorptance, α	0.87	-
Packed bed thermal emittance, ε	0.87	-

3.4 Curtain Development

The curtain thickness changes with the position along the y-axis [see Fig.9]: the more the position is at the bottom of the receiver, the thicker the curtain. The calculation of the curtain thickness has been computed through the Eq.(1)-(2).

$$t_c(y) = t_{c,0} + 0.0087 \cdot y \tag{1}$$

$$t_{c,0} = \left(\frac{60\ \dot{m}}{62\ W_c\ \varphi_{p,0}\ \rho_p\ \sqrt{g}} \right)^{\frac{1}{1.5}} + 1.4 \cdot d_p \tag{2}$$

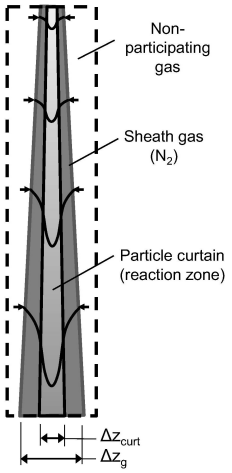

Figure 9: *Particle curtain development along y-axis. [44]*

3.5 Mass and Momentum Balance

As in the curtain thickness computation, the N subdivisions have been applied to the mass balance [Eq.(3)] and momentum balance [Eq.(4)]. The Eq.(3)-(4) are used to define v_p and φ_p at the outlet of each N subdivision, knowing the values at the outlet. The code has been indeed implemented in order to start the balances from the bottom to the top, being the outlet conditions a boundary condition. Then, the particle mass flow rate is calculated iteratively in order to match the inlet conditions.

$$\frac{-\Delta\left(\varphi_p\ t_c\ \rho_p\ v_p\right)}{\Delta y} = 0 \tag{3}$$

$$\frac{-\Delta\left(\varphi_p\ t_c\ \rho_p\ {v_p}^2\right)}{\Delta y} + \varphi_p\ \rho_p\ t_c\ g = 0 \tag{4}$$

3.6 Energy Balance

As for the mass and momentum balance, the known conditions are the ones at the outlet of the receiver as the outlet particles temperature is one of the operational parameter. The same approach was then applied: energy balances for each N subdivision have been carried out from the bottom to the top of the receiver.

$$\frac{-\Delta\left(\varphi_p\ t_c\ \rho_p\ v_p\ h_p\right)}{\Delta y} + g_{c,front} - j_{c,front}\ + \cdots$$
$$\cdots + g_{c,back} - j_{c,back} - q_{adv}^{''} = 0 \tag{5}$$

Irradiances $g_{c,front}$ and radiosities $j_{c,front}$ are defined by Eq.(6)-(9); the advection losses $q_{adv}^{''}$, equation (10), are defined as the product between the temperature difference between the particles and the ambient and the advection heat transfer coefficient. In [7] the value of htc_{adv} changes all along the curtain depending on the position along y-axis. For simplicity, throughout this model the value has been kept constant. The value chosen comes from the reference of the model: the authors have evaluated the coefficient with CFD simulations on both small and commercial scale receivers. The value chosen is the one related to commercial scale receivers, given the large diameter of the component modelled, so the results are expected to be conservative. The htc_{adv} depends on the particle curtain surface and more precisely on its length: higher heights lead to higher particle velocities and higher heat transfer coefficients as well. Worth of notice is the larger the receiver the higher the view factor as well, as it is shown in Ref.[7]. The highest value (F=0.9) has been assumed in order to take into account the worst case scenario as a reference case.

$$g_{c,front} = C_{geo}\ \eta_{hel}\ DNI \tag{6}$$
$$j_{c,front} = F(\varepsilon_c\ \sigma\ {T_p}^4 + \rho_c\ g_{c,front} + \tau_c\ g_{c,back}) \tag{7}$$
$$g_{c,back} = j_w \tag{8}$$
$$j_{c,back} = \varepsilon_c\ \sigma\ {T_p}^4 + \rho_c\ g_{c,back} + \tau_c\ g_{c,front} \tag{9}$$
$$q_{adv}^{''} = htc_{adv}(T_p - T_{amb}) \tag{10}$$

The parameter C_{geo} in Eq.(6) is defined by the ratio between the heliostat field reflective surface and the particle curtain surface.

$$C_{geo} = \frac{Heliostat\ reflective\ surface}{Particle\ curtain\ area}$$

In order to compute the energy balance in the curtain, the energy conservation balance equation, applied to the back wall, is required. In Eq.(11), k_{bw} is the back wall conductivity, T_{bw} is the back wall temperature, g_{bw} and j_{bw} are respectively the irradiance and the radiosity of the surface. The term related to the convection losses between the back wall and the ambient is then represented by $q_{cv}^{''}$, computed through relation in Eq.(14). The conduction in the *y* direction have been calculated using the finite difference method.

$$\frac{d}{dy}\left(k_{bw}\frac{dT_{bw}}{dy}\right) + g_{bw} - j_{bw} - q_{cv}^{''} = 0 \tag{11}$$
$$g_{bw} = j_{c,back} \tag{12}$$
$$j_{bw} = \varepsilon_c\ \sigma\ {T_{bw}}^4 + (1 - \varepsilon_c) g_{bw} \tag{13}$$
$$q_{cv}^{''} = htc_{cv}(T_{bw} - T_{amb}) \tag{14}$$

In Tab.[5], some values used for the calculation are resumed.

Table 5: *Summary of values used for calculation.*

Parameter	Value	Reference
Heliostats efficiency, η_{hel}	0.5	assumed
DNI	750 $\frac{W}{m^2}$	assumed
View factor, F	0.9	[7]
Advection HTC, htc_{adv}	95 $\frac{W}{m^2 \cdot K}$	[7]
Convection HTC, htc_{cv}	10 $\frac{W}{m^2 \cdot K}$	[7]
Heliostats area	$1 \times 10^6\ m^2$	assumed

Optical properties of the particle curtain, transmissivity τ_c, reflectivity ρ_c and absorptivity α_c, have been computed through the model described in "Analysis of optical properties in particle curtains (2021) [52]" by González-Portillo, Luis F. Abbas et al. The model has been then validated in Sec. [3.7.1] in order to verify the results of the overall modelling of the receiver. Each property, has been calculated for each subdivision along the y direction.

3.7 Model Validation

For the model validation, values from the references have been set in the code in order to verify whether the results turned out consistent.

3.7.1 Optical Properties Validation

Regarding the optical properties, the results got were extremely close to the ones from the reference through which the codes have been implemented. In the paper, two different particles have been investigated: sand and bauxite. The difference between the two stands in the absorptivity of the particle, which is equal to $\alpha_p = 0.34$ for sand and to $\alpha_p = 0.87$ for bauxite proppants. The value φ_v is the solids volume fraction, the density of particles in a specific control volume: this parameter should change along the curtain because of fluid dynamics; in this paper,the particle curtain is assumed to be "static", indeed the φ_v value is kept constant. Two values are investigated: $\varphi_v = 0.001$ and $\varphi_v = 0.001$. Along the x-axis there is the ratio between the curtain thickness and the particle diameter, which is kept constant in the investigation at the value of $d_p = 300\ \mu m$, whereas the thickness varies between 0 and 0.48 meters. The validation results can be appreciated in Fig. [11]
.

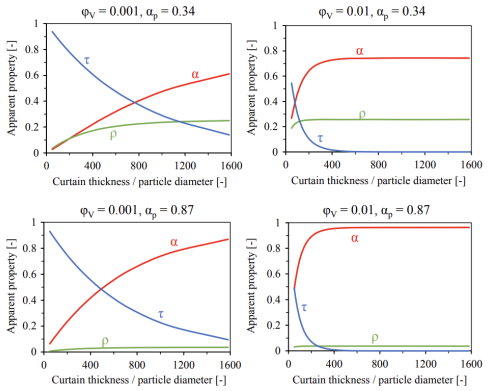

Figure 10: *Optical properties diagram from [52].*

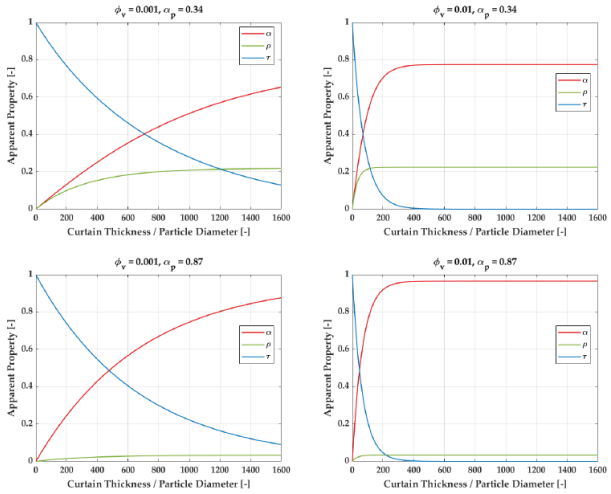

Figure 11: *Optical properties validation diagrams.*

3.7.2 Thermal Model Validation

Regarding the thermal model validation, the reference paper has investigated the losses shares for two different power inputs: $375\ MW$ and $750\ MW$. The particles used for the investigation are the ones resumed in Tab.[4], which have been implemented in the code of the receiver model. The results have shown that with lower curtain areas, the assumption made on the h_{adv} parameter is consistent and the deviation from the original model in Ref.[7] is negligible. The main difference in the model hereby is related to the value of h_{adv}, thus to the advective losses $\dot{Q}_{adv}$, which acquires for the biggest share of the overall receiver losses. In conclusion, the thermal model can be applied for low power inputs as it is consistent with the reference model. For higher input values, an additional implementation of a variable h_{adv} is required.

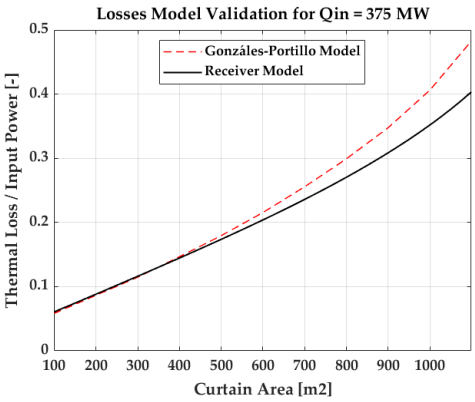

Figure 12: *Thermal model validation, Q_{in} = 375 MW.*

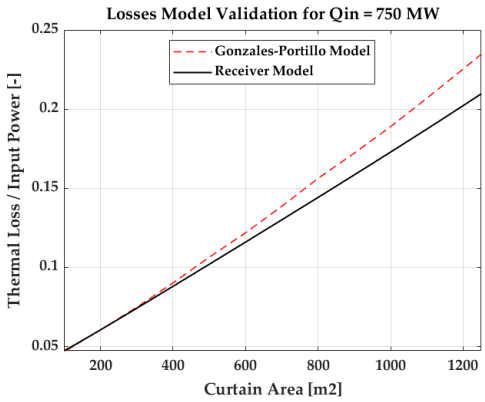

Figure 13: *Thermal model validation, Q_{in} = 750 MW.*

3.8 Receiver Design

3.8.1 Heliostats field

The solar field design has been implemented in SolarPILOT, a comprehensive power tower optical-modelling tool that can also generate different and various field layouts given input constraints or patterns. In addition, the software can also conduct detailed optical performance analysis to the level of each heliostat facet and general optimisation of the primary key parameters. SolarPILOT version (1.4.0) has recently been released and integrated into this model. This new version solves memory issues when working with more than one receiver. In addition, it maximises the total power hitting all receivers rather than trying to satisfy the condition of equal power distribution between the receivers.

Two main configurations have been investigated: a one-receiver tower [Fig.14] and a three-receiver tower [Fig.15] configuration. The one-receiver tower configuration has been first investigated. The specifications for the SolarPILOT model were taken from Ref. [52]. Unfortunately, the results were not satisfying: the higher the number of heliostats, the lower the overall efficiency of the solar field. The low value was due to the significant distance between the tower and the very last mirror row, whose efficiency was extremely low. Notice that, when using cavity receivers, a surrounding field cannot be employed since the cavity receiver only accepts radiation from a range of angles in the horizontal direction. Therefore, polar fields are the only option for one-receiver tower configurations. This poses important problems for large-scale plants, for which a large number of heliostats, and very far from the tower, are needed. All this lead to inefficient operation and, in general, to unfeasible designs. A solution could be employing multiple smaller "north-facing" receivers, but in this work a configuration having three-receiver in the same tower is studied. A fundamental assumption in this model is that all windows in a multi-receiver design have the same area: the receivers are thus of the same size. Other parameters investigated were the tower height and the targeted heliostat field power, thus their number, and how this affected the overall efficiency. The specifications to simulate such solar field in SolarPILOT can be found in Ref. [53]. The three receivers will be facing north, east and west, respectively. The plant is located in Seville and designed for the summer solstice at noon. The design-point DNI is 840 $\frac{W}{m^2}$. An Artificial Neural Network (ANN) trained with SolarPILOT data and capable of reproducing the performance of the three-receiver configuration was provided by the University of Seville. Generally speaking, the network is able to calculate the total power hitting the receivers, the overall optical efficiency of the field and the fraction of the total power hitting each of the three receivers

for different combinations of number of heliostats, tower optical height and receiver height.

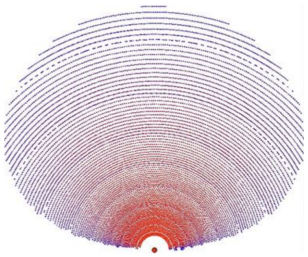

Figure 14: *Sample heliostat field for one receiver. [53]*

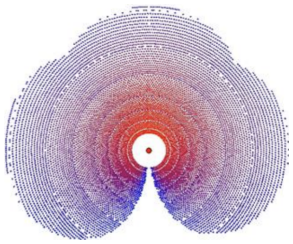

Figure 15: *Sample heliostat field for one receiver. [53]*

The analysis was then carried out defining some optimal parameters for this investigation: the height tower, the azimuth angle and the elevation angle, which is the angle of the sun with respect to the horizon. Value parameter can be found in Tab.[6] and refer to the summer solstice at solar noon in Seville.

Table 6: *Resume of values used for simulation in SolarPILOT.*

Parameter	**Value**	**Unit**
Tower height	200	m
Azimuth angle	121.4	°
Elevation angle	64	°
DNI	840	$\frac{W}{m^2}$

Figure 16: *North, East and West facing three-receiver tower solar field simulation. [53]*

3.8.2 Receiver Diameter

Regarding the receivers, an analysis on a non-homogeneous irradiance hitting the particle curtains has been carried out. The curtain has been divided into 25 subdivisions, each of which has been characterised by a f_N factor, which indicates the fraction of the overall irradiance hitting the N-th subdivision: the central ones will have the highest share. Irradiance distribution can be appreciated in Fig.[17] for the three receivers.

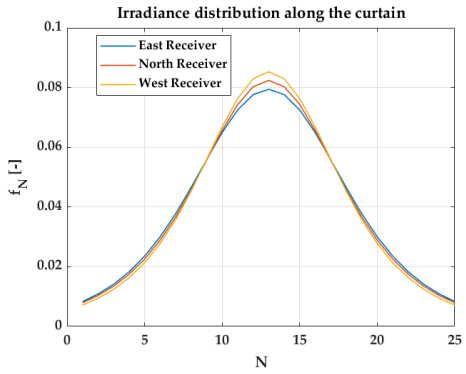

Figure 17: f_N *factor for dishomogeneous irradiance distribution along the curtain.*

Regarding the maximum efficiency of the three-receiver system, it has been found computing separately the three efficiencies of the three receivers and then combining them together through Eq.(15), as if the three components were in a parallel configuration:

$$\eta_{system,rec} = \frac{Q_{in_N}\eta_N + Q_{in_E}\eta_E + Q_{in_W}\eta_W}{Q_{in_N} + Q_{in_E} + Q_{in_W}} \tag{15}$$

Q_{in_i} in the formula is the overall input share for the *i-th* receiver.
The solar field and the receiver efficiencies have then been combined multiplying them together to find the overall system efficiency (solar field and three-receiver tower). A sensitivity analysis has been carried out by varying then the number of heliostat in the field and last but not least the optimal diameter for the receiver has been found. The analysis [Fig.18] shows that the lower the number of heliostat, the higher the efficiency of the receiver system: this is due to the fact that the input irradiance will be lower and so the overall losses. The optimal diameter is kept in the range between 18 and 20 m and the lower the number of heliostat, the lower the optimal diameter.

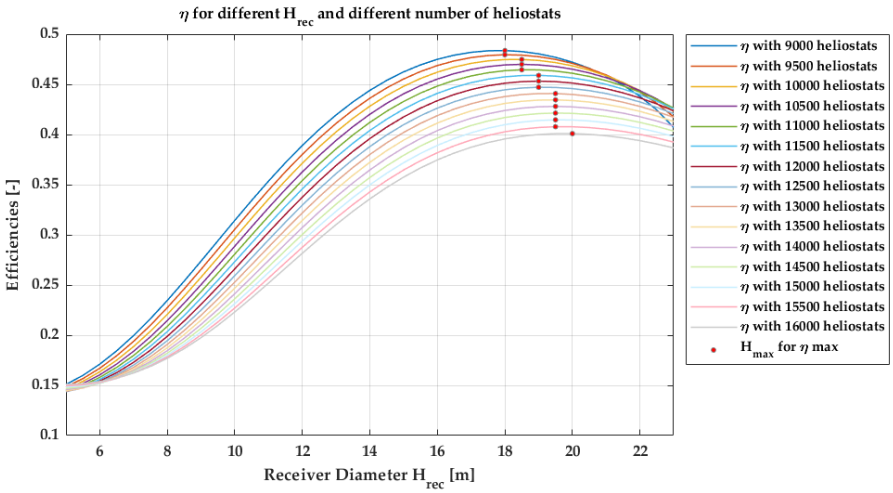

Figure 18: *Sensitivity analysis on* H_{rec} *and on the number of heliostat.*

3.8.3 Design results

Eventually, in order to get the highest performance and to have lower costs of investment, it has been decided to adopt a configuration with 9000 heliostats and a receiver diameter of 18 meters.

The final design results are shown in Tab.[7].

In order to prove the choice of the number of heliostat, a further analysis has been carried out, studying the correlation between the power input and different number of heliostats: surely, the total power input depends proportionally on the total reflective surface, thus on the number of heliostats. However, to be considered a reasonable value, the total power input should be higher than 600 MW in order to reach targets on the power side and have enough thermal energy to reach the working fluid temperature of 700°C at the inlet of the turbine. As shown in Fig.[19], the target value of 600 MW is reached with 8300 heliostats. Extremely high values of total power input can be reached; however, to maximize the system (solar field an three-receiver tower) efficiency the right number of heliostat is the one chosen eventually in the design, thus 9000 heliostats. Higher numbers lead also to higher investment costs, due to the large material involvement, and higher variable costs for the mirror maintainance, which may affect the LCOE of the technology.

Table 7: *Final design values for the receiver.*

Parameter	**Design Value**
Power input, Q_{in}	638.17 MW
Number of receivers	3
Number of heliostats	9000
Heliostats reflective area	12 m^2
Heliostats efficiency, η_{hel}	58.62 %
3-receiver efficiency, η_{3rec}	81.5 %
System efficiency η_{sys}	47.78 %
DNI	840 $\frac{W}{m^2}$
Curtain width, W_c	18 m
Curtain height, H_c	18 m
Curtain area	360 m^2
Particle diameter, d_p	350 μm
Particles	CARBO ID50 [4]
Wall thickness, th_w	0.05 m
Wall thickness, th_{bw}	0.05 m
Aspect ratio, AR	1
Curtain - BW view factor, F	0.9
Advection HTC, htc_{adv}	95 $\frac{W}{m^2 \cdot K}$
Convection HTC, htc_{cv}	10 $\frac{W}{m^2 \cdot K}$

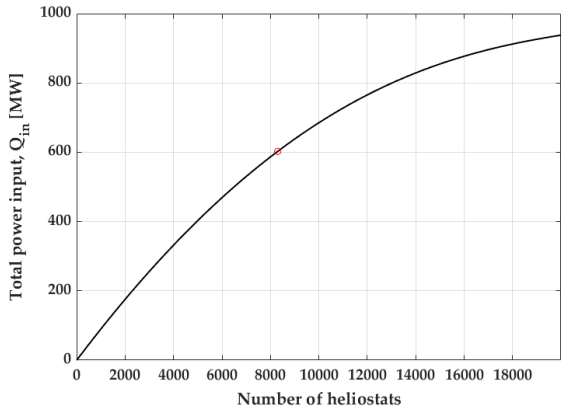

Figure 19: *Sensitivity analysis on the number of heliostats and the total power input.*

3.8.4 Off-design results

An analysis was conducted to assess the off-design efficiency of the falling particle receiver modelled. Efficiency was calculated for each input value [see Fig.20], while varying the receiver height. The results indicate that lower receiver heights generally lead to higher efficiency. The study also identified the minimum power input required for different receiver heights, and thus different particle curtain area which in the model is related to the receiver height, H_{rec}. The greater the characteristic length and the curtain size, the greater the minimum power input that is needed.To achieve a defined outlet particle temperature, the mass flow rate is reduced when power input is small, considering the limits given in the model.

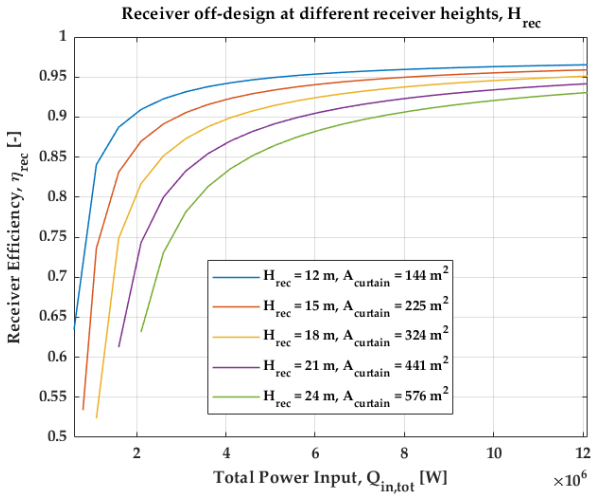

Figure 20: *Receiver off-design efficiency, η_{rec} at different receiver height, H_{rec}.*

Similar findings were reported by González-Portillo in Ref.[54]. The study shows that receiver efficiency increases sharply with small heat fluxes, and more gradually as heat fluxes increase. To achieve the highest efficiencies, heat fluxes above 0.7 $\frac{MW}{m^2}$ are typically required, at which point efficiency curves have a plateau. The paper also highlights that falling particle receivers require higher heat flux thresholds compared to molten salts, and receiver efficiency increases

with absorptivity. Low-absorptivity particles not only result in lower efficiency, but also hinder receiver operation when incident solar radiation is low.

4 Particle-to-sCO$_2$ Heat Exchanger Review

The use of supercritical carbon dioxide (sCO$_2$) as a working fluid in power generation systems has attracted increasing interest due to its high thermal efficiency, low cost, and environmentally friendly properties. To achieve optimal performance of sCO$_2$ power systems, the design and performance of heat exchangers, which are responsible for transferring heat between the working fluid and solid surfaces, are crucial. Particle-to-fluid heat exchangers utilise a particulate material as a thermal carrier to transfer heat between the working fluid and solid surfaces. This type of heat exchanger offers several advantages over conventional heat exchangers, including high heat transfer rates, reduced fouling, and improved thermal stability. Therefore, particle-to-sCO$_2$ heat exchangers have become an increasingly popular area of research and development for sCO$_2$ power generation systems [55].

According to SANDIA [56] main future challenges are:

- The particle-side heat transfer, which has not been adequately investigated and applied to primary heat exchangers.
- Material technology, due to the high operating temperatures and pressures which may lead to corrosion or erosion.
- Thermo-mechanical stress to which the material of the components are subject.
- Costs, as LCOE is a very crucial parameter nowadays in order to generate competitive energy to be sold on the market.

The main requirements for this component design are high pressure ($\geq 20MPa$) and high temperatures ($\geq 700C^{\circ}$).

There are several different models and configurations of particle-to-sCO$_2$ heat exchangers availabe that have been proposed and studied in recent years. Packed bed, fluidized bed and entrained flow configurations are among the most common models used for particle-to-sCO$_2$ heat exchangers. In packed bed heat exchangers, particles are contained within a fixed bed and sCO$_2$ is passed through the bed in order to transfer heat. Fluidized bed heat exchangers operate by passing sCO$_2$ through a bed of particles that are fluidized by a fluid, usually air. In entrained flow heat exchangers, particles are entrained in sCO$_2$ and flow through the heat exchanger, where heat transfer between the solid particles and the working fluid occurs.

Recent research efforts have focused on optimizing the design and performance of particle-to-sCO$_2$ heat exchangers. Both experimental and numerical studies have been conducted to investigate the effects of various parameters, such as particle size and flow rate, on heat transfer performance [57]. Additionally, different materials have been used as particles in particle-to-sCO$_2$ heat exchangers, such as graphite, silica, and alumina, to enhance heat transfer efficiency.

In moving packed-bed heat exchangers [see Fig.22], the heat transfer process is complex and depends on various factors, including the properties of fluid-particle *(bulk)* system, the flow pattern, and the geometry of the heat exchanger. To accurately model and predict the heat transfer in these systems, different approaches have been proposed and tested.

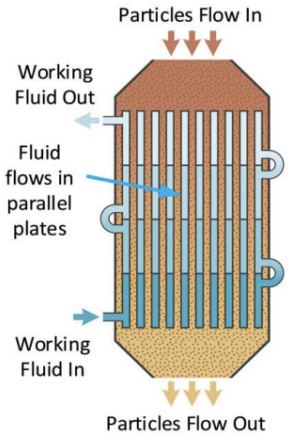

Figure 21: *Moving packed bed heat exchanger. [58]*

Among moving packed bed heat exchangers, it is possible to define two main categories: shell and plate heat exchangers and shell and tube heat exchangers. Overall, modelling the heat transfer in moving packed-bed heat exchangers is a complex task that requires careful consideration of various factors. The approaches mentioned above are just a few examples of the different methods used to tackle this problem, and more research is needed to develop more accurate and reliable models for these systems.

4.1 Fluidized bed heat exchangers

Ma and Martinek provided [58] a model to optimize trade-offs between tube diameter, length and numbers into fluidized bed heat exchanger configuration. A fluidized bed heat exchanger utilizes solid particles that are filled into the tube side or shell side of the exchanger and fluidized by a fluid flowing in the pipe. This fluidization process causes the particles to constantly collide with the wall of the heat exchange pipe, resulting in a scouring effect on the heat exchange wall surface. This scouring effect enhances the heat transfer process between the fluid and the particles, leading to highly efficient heat exchange [59]. Despite the scouring effect, the solid particles will not cause serious wear to the pipe wall due to their small size and low velocity. However, it is important to choose appropriate materials for the heat exchange wall surface that can withstand the abrasion from the fluidized particles over time in order to maintain the longevity of the fluidized bed heat exchanger. In the report from Ma and Martinek, a sensitivity analysis is performed to determine the impact of critical design parameters on the cost of the heat exchanger. Design directions are provided to minimize the heat transfer area and reduce material cost. The low heat transfer coefficient between solid particles and tubes poses the primary heat transfer resistance. However, fluidized beds are able to achieve a high overall heat transfer coefficient due to particle mixing and periodic contacts with heat transfer surfaces. Simulation models were developed based on a counterflow heat exchanger configuration and the results suggest that a solid-side heat transfer coefficient higher than 500 $\frac{W}{m^2K}$ is critical to meet the heat exchanger cost target.

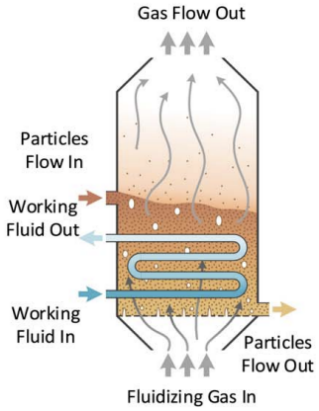

Figure 22: *Fluidized bed heat exchanger. [58]*

4.2 Shell and plate moving packed bed heat exchanger

The Shell-and-Plate moving packed-bed particle-to-sCO_2 (SPMP) is a unique type of heat exchanger that is designed to transfer heat between a stream of solid particles and a supercritical carbon dioxide (sCO_2) stream flow. This heat exchanger consists of a shell-and-plate assembly with a moving packed bed of solid particles that come into contact with the sCO_2 stream flow, allowing heat to be transferred between the two. The design of this heat exchanger is particularly useful for high-temperature applications, such as power generation and industrial processes, where traditional heat exchangers may not be effective due to the limitations of the working fluids used. This configuration is an innovative and efficient solution for heat transfer in demanding applications. The heat transfer process in the SPMP is complex and challenging to model accurately, thus requiring sophisticated approaches. One approach is to use a continuum model, where the fluid and particle phases are treated as a continuous medium with averaged properties. Albrecht and Ho [57, 57] presented a single-component continuum approach model for the heat transfer in a moving packed-bed heat exchanger. They solved the Nusselt numbers using analytical solutions under constant temperature and heat flux boundary conditions. The results showed that the Nusselt numbers were asymptotic to constant values at high residence times in a bounded domain, which contradicts the general thought that the heat transfer coefficient significantly decreases at high residence times. Another approach is to use a two-region model, which divides the near-wall region from the bulk, and assumes different effective thermal conductivities for each area. Botterill and Denloye (2010) [60] developed a two-region model for the heat transfer in a stationary packed-bed. The near-wall region typically has a lower effective thermal conductivity due to higher voidage than the bulk. However, this approach may not be suitable for moving packed-bed heat exchangers, where the flow and packing density can vary significantly. Another modelling approach is the analytical one, which can provide quick and straightforward solutions to estimate the SPMP's performance under different operating conditions. Analytical models are based on mathematical equations that describe the heat transfer process; they can be used to predict the thermal efficiency, pressure drop, and other performance parameters. Fang, Wenchao, et al. [61] investigated the heat transfer characteristics of a shell-and-plate moving packed-bed heat exchanger using continuum modelling. The local heat transfer coefficient was found to drop quickly at the thermal entry region and constant value within the central part of the receiver, with the asymptotic value slightly increasing with particle flow velocity but decreasing with particle channel width. A universal relationship between the local heat transfer coefficient and particle flow properties was proposed in terms of the dimensionless Nusselt number and Graetz number. The performance of

the heat exchanger was evaluated over a wide range of input parameters, and a sensitivity analysis was performed to determine the parameters that play a dominant role in the overall heat transfer coefficient and the outlet temperature of the sCO_2 flow. A two-regime behavior of the overall heat transfer coefficient was reported, with the performance of the heat exchanger mostly depending on particle flow velocity and channel width in the low flow rate regime, while effective particle flow conductivity becomes the determining factor in the high flow rate regime. These approaches can provide valuable insights into the SPMP's thermal and hydraulic performance, which can be used to optimize its design and operating parameters. The references cited in this paragraph provide further information on the modelling of the SPMP and its applications in various industries. The shell-and-plate, moving packed-bed, particle-to-sCO_2 heat exchanger is a promising technology for high-temperature heat recovery systems, but its design and operation must be carefully considered to achieve optimal performance.

4.2.1 Purely counter-flow shell and plate heat exchanger

In this configuration [see Fig.24], proposed by Ho [3], particles enter the heat exchanger from the top and flow downwards driven by gravity through narrow channels in between parallel plates, whereas the sCO_2 flow enters the heat exchanger from the bottom and flows up through hundreds of microchannels within the parallel plates. A thermomechanical model is then proposed by DeLovato in 2022 [62]. The design was modeled to determine thermal performance and mechanical stress during steady-state and transient operation. The modeling technique resolved full 3-D geometries, which predicted an improvement in the overall heat transfer coefficient by over 160% compared to a cross-flow design. The model also identified areas within the plate that were in poor thermal communication and high induced stress during transient operation. Further development of the model involves implementing a computational fluid dynamics analysis of the sCO_2 flow in the microchannel plates and a detailed analysis of induced stress around the edges of the microchannels.

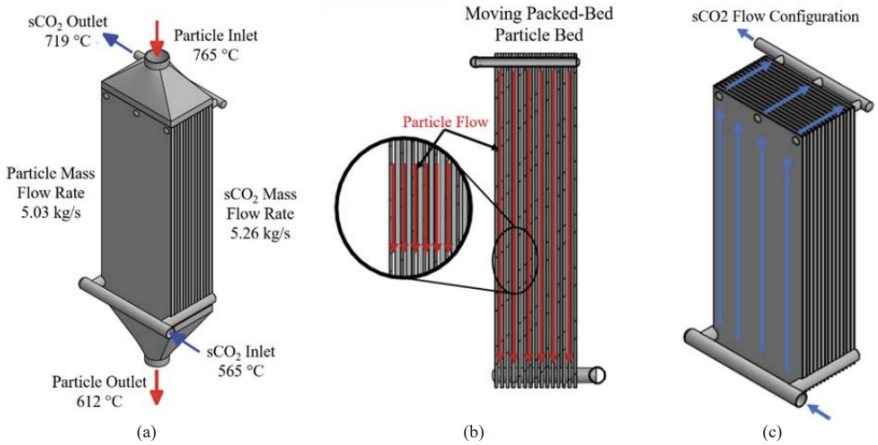

Figure 23: *Proposed configuration in [3, 62]*

4.2.2 Global counter-flow with local cross-flow shell and plate heat exchanger

In this configuration proposed by Albrecht and Ho in Ref.[63], the heat exchanger consists of several banks of parallel plates arranged in a vertical orientation. The global flow configuration of the heat exchanger is in a counter-flow setup, where sCO_2 (supercritical carbon dioxide) flows in a serpentine fashion through the parallel plates from the base to the top of the heat exchanger.

This means that the sCO_2 and the particles flowing in the opposite direction come into contact with each other, allowing for heat transfer to occur. However, within each individual bank of plates, the flow configuration is in a cross-flow setup. This means that the sCO_2 flows horizontally in the heat transfer region, while the particle flow is in the vertical direction. The particles flow downward in between the parallel plates under the force of gravity, creating a dense granular regime. Despite the good contact between the particles and the heat transfer surface, the heat transfer from the high-temperature particles to the sCO_2 contained in the parallel plates is limited by the relatively low thermal conductivity of the particle bed. In [63] a reduced order model has been developed for a moving packed-bed heat exchanger to be used for particle-to-sCO_2 heat transfer in next-generation CSP plants. The methodology captures the necessary physics for dense granular flow heat transfer while being lightweight enough for use in parametric studies. The importance of selecting particle size and channel geometry together was established, with trade-offs in near-wall thermal resistance and thermal conductivity of the packed bed observed. In the investigation, overall heat transfer coefficients approached a value of $400 \frac{W}{m^2 K}$. Improvements in particle thermophysical properties, such as thermal conductivity and packed bed void fraction, could lead to significant improvements in overall heat transfer coefficient.

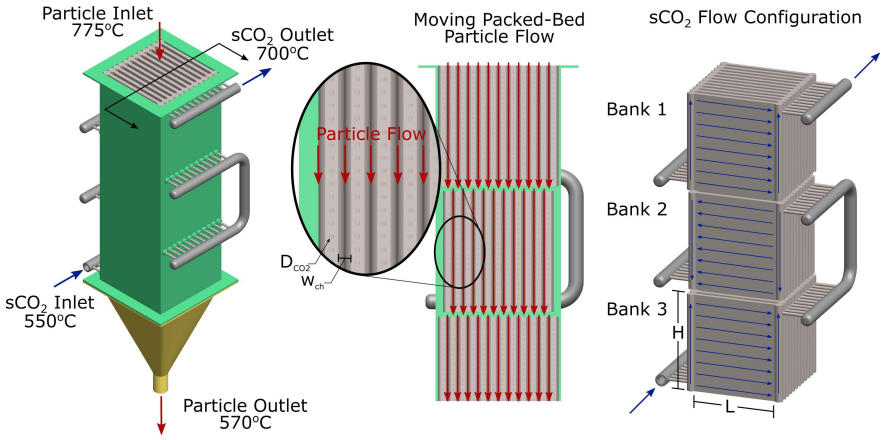

Figure 24: *Design of a shell and plate configuration proposed in Ref.[63].*

4.3 Shell and tube heat exchanger

Shell and tube heat exchangers have been used for many years in various industrial applications. However, with the increasing demand for more efficient and environmentally friendly energy sources, the focus has shifted towards developing advanced heat exchanger technologies. One such technology is the shell and tube particle-to-sCO_2 heat exchanger. The design of shell and tube particle to sCO_2 heat exchangers is based on the concept of indirect contact heat transfer between the working fluid, supercritical carbon dioxide (sCO_2), and a stream of solid particles. The heat transfer occurs as the sCO_2 flows through a tube bundle, and the solid particles are injected. The sCO_2 absorbs the heat from the hot particles, heating the fluid up before it goes to the power cycle. The design parameters for this type of heat exchanger include the particle size, flow rate, and tube diameter and heat transfer coefficient on the particle side. The design of shell and tube particle to sCO_2 heat exchangers is typically performed using computational fluid dynamics (CFD) simulations. The performance of shell and tube particle to sCO_2 heat exchangers is evaluated based on several parameters such as the heat transfer coefficient, pressure drop, and overall heat transfer coefficient. The last is a measure of the heat transfer efficiency of the heat exchanger

and is calculated by taking into account the resistance to heat transfer on both sides of the heat exchanger, particles and fluid. The pressure drop, which is the difference in pressure between the inlet and outlet of the heat exchanger, is another crucial parameter as it determines the pumping power required to circulate the sCO_2 flow. The performance of shell and tube particle to sCO_2 heat exchangers can be improved by optimizing the particle injection method, the tube geometry, and the heat transfer coefficient.

Ammar Ali Abd, Mohammed Qasim Kareem, Samah Zaki Naji in Ref. [64] examined how altering certain parameters impacted the heat transfer coefficient and pressure drop in a shell and tube heat exchanger. The findings indicated that enlarging the shell diameter led to a rise in both the heat transfer coefficient and pressure drop. However, the heat transfer coefficient was diminished as baffle spacing and cutting space were increased. Moreover, the fouling factor on the shell side was found to affect heat transfer more than the tube side.

In Ref.[65] the authors confirmed a correlation between fluid velocity and heat transfer coefficient through numerical calculations. The outcomes indicate that increasing flow rates result in higher heat transfer coefficients. However, it is important to note that high velocities can lead to elevated pressure drops, potentially shortening the lifespan of equipment. Furthermore, a new correlation has been proposed using Kern's method to improve the accuracy of the results of the overall performance.

Too, Yen Chean Soo, et al. in Ref.[66] proposed a new configuration for shell and tube heat exchangers [see Fig.25]. The design involves a vertical tube array in a counter-flow heat exchanger that maximizes the use of the tube's entire outer surface for heat transfer. It uses solid particles falling under gravity along the outer surface of the tubes, which provides a high surface area for heat transfer and reduces fouling. This design can operate at higher temperatures and pressures than traditional heat exchangers and is suitable for high-temperature applications, such as in power generation systems. Overall, this particle heat exchanger design offers a more efficient and effective solution for heat transfer in industrial processes. To make larger scale heat exchanger systems practical and economically viable, the number of tubes can be reduced by using long tubes along with a higher mass flux design. However, poor particle-side heat transfer still presents a challenge in designing an efficient heat exchanger.

Computational fluid dynamics (CFD) is another powerful tool for modeling the heat transfer in moving packed-bed heat exchangers. Baumann and Zunft (2015) in Ref.[67] used CFD analysis to simulate the hydrodynamics of a moving packed-bed heat exchanger. They used an Eulerian-Eulerian model to capture the velocity profile around the tubes but not in the void zone below the tubes. The results showed good agreement with experimental data and suggested that the Eulerian-Eulerian approach is suitable for properly simulating moving packed beds. Gas phase thermal conductivity has also been shown to have a significant impact on the heat transfer in packed-bed heat exchangers, especially under pressurized conditions. Additionally, using particles with increasing volume fraction to reduce voidage in the bulk and near-wall regions can enhance the heat transfer process.

A two-dimensional heat transfer model was developed and validated against experimental results. The study showed that granular particles become thermally fully developed once they travel a certain distance from the inlet, and an increase in particle velocity does not significantly increase particle-to-wall heat transfer coefficient for PHX lengths longer than 1m. In conclusion, the shell and tube particle to sCO_2 heat exchanger is a promising technology for improving the efficiency and performance of power generation systems. By using direct contact heat transfer between particles and sCO_2, this type of heat exchanger can achieve higher heat transfer rates and reduce the size and weight of the overall system.

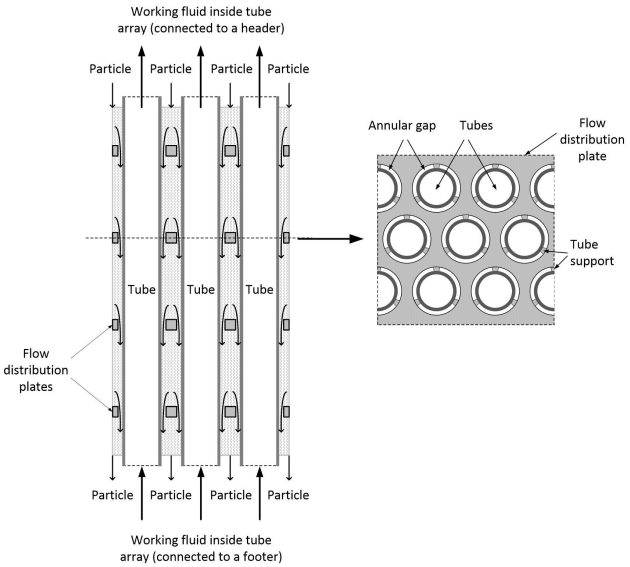

Figure 25: *Shell and tube configuration proposed in Ref.[66].*

Although further research is needed to fully understand the performance and reliability of this technology, the current literature suggests that it has great potential for enhancing the efficiency of power generation systems. Heat transfer modelling, tests, and cold model flow tests have shown promising results for the new design. Preliminary experimental results with the first attempt at a flow constrictor design showed an approximately 43% enhancement in particle-side heat transfer for a staged HX. However, there is room for improvement in design to maximize particle-side heat transfer by achieving better mixing between stages and full renewal of thermal entrance zone effects at each stage.

4.4 Final considerations

Regarding final considerations, given the information from the references it is possible to state that all three technologies are promising reaching the goal for the next-Gen CSP power plants involving sCO_2. Fluidized bed and shell and tube configuration have proved to be very competitive and promising technologies to be coupled with sCO_2. However, the shell and tube configuration seemed the more interesting as the heat transfer on the particle side is still a challenging topic. Some studies have been carried out by Bartsch in Ref.[68] and earlier by Hertel and Zunft in Ref.[69]. The latter study reported found that the predicted heat transfer coefficients (HTCs) by the simulation model were generally in good agreement with experimental results, particularly in the area-weighted HTCs, which are important for design purposes. However, some deviations were observed in local HTC curves at the top and bottom of the tube where stagnation and void zones are located. These deviations were attributed to an overestimation of the reduction in heat transfer in these zones. Nevertheless, the level of accuracy is still considered adequate for design purposes and fills a gap in the development of gravity-driven moving bed heat exchangers and particle-based solar power plants. The uniform particle flow distribution allows a good effectiveness and a better heat transfer, when compared to non-homogeneous flows as in shell and plate configurations, also due to thermal gradients and warping of plates that may characterize this category of heat exchangers.

Furthermore, as explained in Tab.[8] and [9], shell and tube do not involve nozzles and fluidization of the particle bed which in case of the shell and plate and fluidized bed heat exchanger

introduce parasitic losses. With an optimal design, it is possible to get an high heat transfer area with compact geometries, a high efficiency and low pressure drops: these targets are essential for the downstream power block and to achieve working fluid targets, regarding temperatures and pressures.

Table 8: *Final Comparison between HX Configurations*

HX Design	**Pros**	**Cons**	**Risk Mitigation**
Fluidized Bed HX	High U values (see Table 9); low heat transfer area.	High parasitic power and high heat loss from gas fluidizing.	Minimization of fluidization velocity to reduce power requirements and heat loss through CFD modelling.
Shell and Tube HX	Gravity-driven flow and high-pressure tube handling; low pressure drops in tubes.	Particle flow stagnation area on top of the tubes and shadow beneath the tubes may impede heat transfer.	Particle side heat transfer to be improved; evaluation of tube configuration (such spacing between tuber or more surface for heat transfer).
Shell and Plate HX	Gravity-driven flow and high potential surface area for direct particle contact; high U values due to narrow channels.	Thermal gradients and warping of plates, numerous nozzles. Potential for non-uniform particle flow.	Use of multiple plate banks to minimize thermal gradient, proper spacing of plates, and adequate thermal insulation around nozzles.

Table 9: *Comparison on the U value.*

Design HX	**U value** $\frac{W}{m^2K}$
Fluidized Bed HX	$>$500 [48]
Shell-and-Plate Moving Packed Bed HX	400 [63]
Shell-and-Tube Moving Packed Bed HX	240 [67]

5 Heat Exchanger Model

Based on the final consideration in Sec.[4.4], a cross flow shell and tube configuration is adopted and therfore modeled. A heat transfer model [Ref.[68]] for the particles bulk is applied and will be fully described in the following part of this report. The particles taken into account are the ones for the receiver, as the primary heat exchanger is supposed to be downstream of the falling particle receiver in systems that are not provided with a TES system.

5.1 Equations and correlations

5.1.1 Energy balance

Basic energy balance equations have been applied to the fluid (16) and to the particle side (17).

$$\dot{Q} = \dot{m}_{WF}(h_{WF}^{out} - h_{WF}^{in}) \tag{16}$$

$$\dot{Q} = \dot{m}_p c_{p,av}(T_p^{in} - T_p^{out}) = \dot{m}_p \int_{T_{out}}^{T_{in}} c_p(T)dT \tag{17}$$

These two equations (16)-(17) have been used to compute the overall energy transferred, $\dot{Q}$, and the particle mass flow rate, $\dot{m}_p$.

5.1.2 Heat transfer

For the heat transfer equations, in first place $\dot{Q}_{max}$ has been computed through a numerical evaluation with Eq.(19), (20)-(21) in order to calculate the effectiveness ε_{HX} of the heat transfer with Eq.(18).

$$\dot{Q} = \varepsilon_{HX} \cdot \dot{Q}_{max} \tag{18}$$

$$\dot{Q}_{max} = min\left[\dot{Q}_{max}^1, \dot{Q}_{max}^2\right] \tag{19}$$

$$\dot{Q}_{max}^1 = \dot{m}_p c_p({T_p}^{in} - {T_{WF}}^{in}) \tag{20}$$

$$\dot{Q}_{max}^2 = \dot{m}_{WF} \cdot (h({T_p}^{in}, {P_{WF}}^{out}) - {h_{WF}}^{in}) \tag{21}$$

Heat exchangers are governed by relative simple equations that may vary, depending on the different arrangements of the flows. In order to compute the NTU, number of transfer units, unmixed flows and crossflow arrangement is assumed.

$$\varepsilon = f(NTU, R) \tag{22}$$

$$R = \frac{C_{min}}{C_{max}} = \frac{(\dot{m}c)_{min}}{(\dot{m}c)_{max}} \tag{23}$$

After the computation of the NTU with Eq.(22)-(23), it is possible to calculate the parameter UA, which is the product between the overall heat transfer coefficient and the tubes external heat transfer surface, using Eq. (24). The overall heat transfer coefficient *U* is a crucial parameters as the higher it is, the higher and the better the heat transfer process is. U has been computed through Eq.(25). Regarding the heat transfer coefficient h_{WF} on the working fluid side, the Gnielinski correlation has been applied, since it is flowing in circular tubes. All working fluid properties have been computed considering both pressure and temperatures averages between inlet and outlet conditions. For the particles heat transfer coefficient h_p a whole section (see Sec.[5.2]) has been dedicated to the modelling.

$$NTU = \frac{UA}{(\dot{m}c)_{min}} \tag{24}$$

$$U = \frac{1}{\frac{1}{h_p} + \frac{D_o \cdot ln\left(\frac{D_o}{D_i}\right)}{2k_T} + \frac{D_o}{h_{WF} D_i}} \tag{25}$$

The parameter k_T in Eq.(25) is the conduction of the tubes material. In the code developed, the possibility to change the material has been implemented, although only few material have been validated for these applications.

5.1.3 Heat exchanger geometry

Geometry design values, such as the tubes external surface (see Eq.(26)) and the total length of the tubes (see Eq.(27)), have been computed and included in the code as well: these parameters are crucial for the design of this component.

$$UA = A_{out,tubes} \cdot U \tag{26}$$

$$A_{out,tubes} = L_{tubes}\ \pi\ D_o \cdot n_{tubes} \tag{27}$$

Regarding the tubes, based on the material and different operating parameters, different thickness can be computed. The formula implemented takes into account a safety parameter k_{saf} which is considered extremely important for high pressure applications. Its value should be between 1.3 and 2 depending on the application; in this case a value of 1.5 has been applied.

$$th_{tube} = k_{saf}\left[\frac{P_{des,max}D_{out,t}}{2\sigma(T_{wall} + P_{des,max})} + 0.005D_{out,t}\right] \tag{28}$$

$$h_{WF}A_i(T_{wall} - T_{WF}) = h_pA_o(T_p - T_{wall}) \tag{29}$$

Eq.(28) depends also on the temperature of the tubes wall, which has been computed through an energy transfer balance between the particle on the outside surface of the tubes and the working fluid flowing and wetting the inner surface of the tubes (see Eq.(29)).

5.1.4 Pressure losses

Regarding the pressure losses in order to design the heat exchanger, a target has been previously defined. To verify whether the target has been respected (with Eq.(30)), the velocity of the working fluid in the tubes is computed with Eq.(33). All fluid properties have been computed considering both pressure and temperatures averages between inlet and outlet conditions: these assumptions may not be totally accurate but the deviation will be low, given the high operational temperatures and pressures. Reynolds number and Darcy friction factor calculation have been computed with the averaged fluid properties with Eq.(32) and (31). The Darcy friction factor has been computed through the Colebrook relation.

$$\Delta P_{WF} = f_{Darcy}\frac{L}{D_i}\frac{\rho v^2}{2} \tag{30}$$

$$f_{Darcy}\left(Re, \frac{\varepsilon}{D}\right) \tag{31}$$

$$Re = \frac{\rho v D_i}{\mu} \tag{32}$$

$$v = \frac{\frac{\dot{m}_{WF}}{RT}}{\pi\rho\frac{{D_i}^2}{4}} \tag{33}$$

5.1.5 Particle velocity

Particle velocity, which is affected by the gravity force, can be easly found with the following Eq.(34).

$$v_p = \frac{\dot{m}_p}{\rho_{bulk}L_{tube}N_{col}s_H} \tag{34}$$

This equation will be useful for the model validation, held in Sec.[5.3].

5.2 Particles heat transfer coefficient h_p modelling

Granular materials, like tiny particles, are in a two-phase system. In this case study, the particles are surrounded by air, which hugely affects the thermal and fluid-dynamics properties of the whole bulk. Throughout the past years, different approaches have been developed to study fluidized packed bed flows. They mainly belong to two groups: discrete particle models, which consider the material as distinct particles which will be followed one by one, and continuous models, in which the material is treated as a continuous medium.

The approach to model the heat transfer coefficient on the particle side is Bartsch's [see Ref.[68]]. His model follows and improves the model of Niegsch [see Ref.[70]], who was the first to study the heat transfer between a moving bed and a bundle of horizontal tubes. He investigated different particle materials, observing how the material affects the heat transfer coefficient, which varies along the tube circumference. The HTC not only varies with the velocity but also with the particle's position around the tube. Low heat transfer rates have been observed above and below the tube; however, high heat transfer rates are observed on the lateral sides, where the flow speed detected is higher.
A stagnant area is formed above the tube, increasing the resistance to the heat transfer process between the working fluid flowing in the tubes and the outside fluidized particle falling flow. Below the tubes, a void zone with air but particles is formed due to the circular shape of the tube and the falling particle trajectory: in this area, the heat transfer coefficient observed is lower due to the lack of particles, which notoriously have a higher HTC than gases. Niegsch has then concluded that these two areas should account for two additional thermal resistances in the calculation of the heat transfer coefficient on the particle side. He has developed an empirical model to describe the bulk solid thermal properties and heat transfer process.

As shown in Fig.[26], three different sections around the tube are identified and three different heat transfer coefficients are computed.

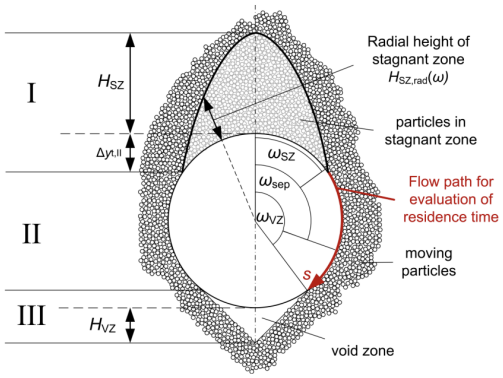

Figure 26: *Tube sections and parameters description. [68]*

Throughout the model in the following section, some parameters appear and therefore they will be introduced hereby: the horizontal spacing of the tubes, s_H, is the length between two different tubes in the horizontal direction; the vertical spacing of the tubes, s_V, is the height between two rows of tubes in the vertical direction; the wall friction coefficient, μ_W, is the inner friction angle and it is assumed in the model because no literature validation exist for bauxite proppants, as stated in the reference; the angle of internal friction, Φ_i, is a crucial parameter on which ω_{VZ} depends (see Eq.(36)). The different values varies with the material of the particle and in case of proppants of

bauxite, it is assumed to be equal to $\Phi_i = 29°$.

$$\omega_{sep} = 120.5° \tag{35}$$

$$\omega_{VZ} = 180° - \Phi_i \tag{36}$$

Regarding the following model, for the two-phase (particle-air) system, the *bulk* thermal properties have been computed according to the model described by Kuipers and developed in 1992 [see Ref.[71]]. This theoretical description is based on a two-fluid model approach in which both phases have been considered as continuous and fully interpenetrating. The model provides thermal conductivity for both bulk and solid parts and it has to be interpreted as effective transport properties. In the following sections, bulk properties will be described with the *S0* subscript, i_{S0}.

5.2.1 Section I

Section I is the so-called stagnant area, because in this zone a thick layer of falling particles is formed. H_{SZ} is the height of the stagnant zone depends mainly on the vertical spacing of the tubes, as Bartsch states in [68], although in the model they are considered only virtual quantities in order to have an approximate description of the magnitude of the height of the stagnant zone. ω_{SZ} is the angular extent of the stagnant area.

$$\alpha_{I,av} = \frac{1}{\left(\frac{1}{\alpha_c}\right)_{I,av} + \left(\frac{1}{\alpha_{S0}}\right)_{I,av} + \left(\frac{1}{\alpha_{SZ}}\right)_{I,av}} \tag{37}$$

However, in this model, for simplification, coefficients α_c and α_{S0} are considered constant:

$$\left(\frac{1}{\alpha_c}\right)_{I,av} = \left(\frac{1}{\alpha_c}\right)$$

$$\left(\frac{1}{\alpha_{S0}}\right)_{I,av} = \left(\frac{1}{\alpha_{S0}}\right)$$

The HTC (see Eq.(37)) is characterised by an additional thermal resistance, called penetration resistance ${\alpha_{S0}}^{-1}$, related to the stagnant zone. It is computed using the residence time (see Eq. (38)) at the beginning of section I.

$$t_{II} = \frac{D_t}{2}\frac{(1 - cos(\omega_{sz}))}{u_{ref}} \tag{38}$$

The conduction resistance, ${\alpha_{SZ}}^{-1}$, depends on the radial height, $H_{SZ,rad}$, which is computed through diagrams interpolations provided in the Bartsch thesis. The parameter integral has been provided in the reference thesis and is found here in Eq.(39). The parameters m and t are defined with the following relations (40)-(41):

$$\left(\frac{1}{\alpha_{SZ}}\right)_{I,av} = \frac{2}{\lambda_{S0}\,\pi^2}\frac{1}{\Delta\omega}\left[\frac{2t \cdot arctanh\left(\frac{m+tan(\frac{\omega}{2})}{\sqrt{m^2+1}}\right)}{\sqrt{m^2+1}} - \frac{D_{tubes}}{2}\,\omega\,\frac{\pi}{180°}\right]_0^{\omega_{SZ}} \tag{39}$$

$$m = \frac{\frac{D_T}{2}\,cos(\omega_{SZ}) - t}{sin(\omega_{SZ})} \tag{40}$$

$$t = H_{SZ} + \frac{D_T}{2} \tag{41}$$

5.2.2 Section II

In this section, the averaged HTC $\alpha_{II,av}$ is calculated as in Eq.(42), and with Eq.(43)-(44)-(45). As in the previous section, the penetration resistance depends on the residence time *t*, which depends on the average velocity in the flow cross section between the tubes. The velocity of the air-particle flow has a constant average value.

$$\alpha_{II,av} = \frac{1}{\left(\frac{1}{\alpha_c}\right)_{II,av} + \left(\frac{1}{\alpha_{S0}}\right)_{II,av}} \tag{42}$$

$$u_{II,av} = -\frac{u_{ref}\ s_H}{\omega_{VZ} - \omega_{SZ}} \left[\frac{2arctan\left(\frac{D_T - s_H\ tan\left(\frac{\omega}{2}\right)}{\sqrt{s_H^2 - D_T^2}}\right)}{\sqrt{s_h + H^2 - D_T^2}} \right]_{\omega_{SZ}}^{\omega_{VZ}} \tag{43}$$

$$\left(\frac{1}{\alpha_{S0}}\right)_{II,av} = \frac{2}{3}\frac{1}{\Delta\omega}\sqrt{\frac{\pi\ D_T}{2(\lambda\ \rho\ c_p)_{s0}\ u_{II,av}}} \left((\omega_0 - \omega_{SZ} + \omega^{''})^{\frac{3}{2}} - (\omega_0 - \omega_{SZ} + \omega^{'})^{\frac{3}{2}} \right) \tag{44}$$

$$\Delta\omega = \omega^{''} - \omega^{'} = \omega_{VZ} - \omega_{SZ} \tag{45}$$

ω_0 is the angle which corresponds the residence time t_0 and depends on the number of row of tubes inside the heat exchanger. In this case it is assumed as a constant value (see Eq.(35)).

The contact resistance is considered constant in the range between ω_{SZ} and ω_{sep}, the angle at which the particles ideally separate from the tube. Between ω_{sep} and ω_{VZ}, the angle at which the so-called void zone begins, the local ratio of the tube surface covered with particles, $\varphi(\omega)$, decreases linearly, as in Eq.(46).

$$\varphi(\omega) = \begin{cases} \varphi_0 = 0.65 \\ \dfrac{\varphi_0}{\omega_{sep} - \omega_{VZ}}(\omega - \omega_{VZ}) \end{cases} \tag{46}$$

The formulation of the contact resistance α_c was then integrated and implemented as in Eq.(47).

$$(\alpha_c(\omega))^{-1} = (\varphi(\omega)\alpha_{WP} + \alpha_{con} + \alpha_{rad})^{-1} \tag{47}$$

5.2.3 Section III

This section of the tube circumference is particular: this is called void area and the heat transfer coefficient mainly depends on the fluid surrounding the particles. Indeed, there is a lack of granular solids. The convective heat transport is computed through Eq.(48). The *Nu* number is computed according to Churchill and Chu correlation (see Eq.(49)-(50)). H_{VZ}, the height of the void zone

under the tubes is computed with Eq.(51).

$$\alpha_{conv} = \frac{\lambda_f}{H_{VZ}} \cdot Nu \tag{48}$$

$$Nu = (0.825 + 0.387 \left(Ra^{\frac{1}{6}} \cdot f(Pr) \right)^2 \tag{49}$$

$$f(Pr) = \left(1 + \left(\frac{0.492}{Pr} \right)^{\frac{9}{16}} \right)^{-\frac{8}{27}} \tag{50}$$

$$H_{VZ} = \frac{D_T}{2} \left(\frac{1}{cos(\Phi_r)} - 1 \right) \tag{51}$$

In the range of $\omega_{VZ} < \omega < 180°$, the convective heat transfer coefficient α_{conv}, is interpolated linearly between as follows:

$$\alpha_{conv}(\omega) = \frac{\alpha_{conv}(180°) - \alpha_c(\omega_{VZ})}{180° - \omega_{VZ}} (\omega - \omega_{VZ}) + \alpha_c(\omega_{VZ})$$

The local effective heat transfer coefficient at the end of the section, so when ω =180°, is found with Eq.(52). In order to compute the average heat transfer coefficient of the section [Eq.(55)], the local effective heat transfer coefficient at the beginning of the section has to be computed [Eq.(53)-(54)].

$$\alpha_{III,loc} = \left(\frac{1}{\alpha_{conv}} + \frac{1}{\alpha_{S0}} \right)^{-1} \tag{52}$$

$$\alpha_{III,loc} = \left(\frac{1}{\alpha_{conv}} + \frac{1}{\alpha_{S0}} \right)^{-1} \tag{53}$$

$$\alpha_c = \varphi \alpha_{WP} - (1 - \varphi) \alpha_{con} + \alpha_{rad} \tag{54}$$

$$\alpha_{III,av} = \frac{\alpha_{III,loc}(\omega_{VZ} + \alpha_{III,loc}(\omega = 180°)}{2} \tag{55}$$

5.2.4 Particles HTC

The final calculation of the heat transfer coefficient on the particle side is evaluated trough in Eq.(56):

$$h_p = \frac{\omega_{SZ} \alpha_{I,av} + (\omega_{VZ} - \omega_{SZ}) \alpha_{II,av} + (180° - \omega_{VZ}) \alpha_{III,av}}{180°} \tag{56}$$

This model tends to underestimate the actual heat transfer, because the penetration resistance is challenging and in the reference is not well defined how the lower rows in the heat exchanger are affected or how the residence depends on the number of the row. However, it is shown how in section II, no stagnation and an appropriate residence time, the penetration resistance increases along with the residence time. The maximum is reached in the beginning of section II.

5.3 Model Validation

The model of the particles-to-CO_2 shell-and-tube heat exchanger has been validated against the one designed by COMPASsCO$_2$ and explained in its Deliverable 1.2 [72] The values of the main variables for the particles and for the working fluid implemented in the code are found in Tab.[10] and in Tab.[11]. Regarding geometrical parameters, they can be found instead in Tab.[12].

Table 10: *Reference particles parameters.*

Bauxite particles		
Parameter	**Value**	**Unit**
Heat capacity, c_p	1200	$\frac{J}{kgK}$
Conductivity, k_p	2	$\frac{W}{mK}$
Density, ρ_p	3550	$\frac{kg}{m^3}$
Diameter, d_p	450	μm
Mass flow rate, $\dot{m}_p$	355.9	$\frac{kg}{s}$
Inlet temperature	900	°C
Outlet temperature	582.8	°C

Table 11: *WF operational parameters.*

Working fluid		
Parameter	**Value**	**Unit**
Inlet temperature	532.8	°C
Outlet temperature	700	°C
Inlet pressure	265.3	bar
Outlet pressure	260	bar
Mass flow rate, $\dot{m}_{WF}$	632.6	$\frac{kg}{s}$

Table 12: *HX operational parameters.*

Parameter	**Value**	**Unit**
Tube diameter, d_{ext}	60.3	mm
Vertical pitch	77.7	mm
Horizontal pitch	69.3	mm
Tube thickness	8.7	mm
Material	Haynes 282 [73]	
Particle velocity	1	$\frac{\mathrm{mm}}{\mathrm{s}}$
Particle HTC, h_p	200	$\frac{\mathrm{W}}{\mathrm{m^2K}}$
Packed volume fraction	0.55	-

The design obtained with the numerical tool hereby developed is compared to the model from the COMPASsCO$_2$ Deliverable [72] in terms of the calculated tube length, number of columns, number of rows and the total external heat exchange area. An excellent estimation of the total transfer area (+0.3%) and the number of rows is observed (0%). On the other hand, the length of the tubes is overestimated (+32%) and the number of columns is significantly underestimated (-24%). These deviations, expressed in the Tab.[13], may indicate that the calculation of the heat transfer is consistent between both of the models, yielding almost the same heat exchange surface. On the other hand, this also shows a discrepancy in the pressure loss calculation model, with lower losses per meter in our model, thus requiring fewer tubes in parallel (number of columns). Unfortunately, there is no information on the model used by COMPASsCO$_2$ in the deliverable.

Table 13: *Validation values regarding the heat exchanger.*

Parameter	Reference Value	Model Value	Unit
Tube length per row	7.8	10.3	m
Number of columns	334	253	-
Number of rows	20	20	-
Total external surface	9870.5	9895.9	m^2

Both the above calculations and the reference model assume that the particle transfer coefficient (h_p) equals 200 $\frac{W}{m^2K}$, which appears to be overestimated. Indeed, it has been found that this value can be much lower for this technology, especially if the particle inlet velocity has such low values as it is 1 $\frac{m}{s}$. Therefore, it has been decided to compare the above design with the one obtained if the assumption that the constant side-particle transfer coefficient is eventually relaxed, and the particle-side heat transfer coefficient is calculated according to the model explained in the reference by Bartsch.

For the sake of comparison, different particle inlet velocities are considered. The results are given in Tab.[14]. First of all, the overall heat transfer coefficient *U* turns out to be much lower, from 166.43 $\frac{W}{m^2K}$ to 65.4 $\frac{W}{m^2K}$, confirming the previous hypothesis of the overestimated parameter in the deliverable reference by COMPASsCO$_2$. As a consequence of this, the total external heat exchange area significantly is increased (+154%). The number of rows also increases significantly from 20 to 51. As a result of a greater total piping length, which is product of tube length per row and the number of rows, the number of columns must increase to reduce the circulation mass flow rate and therefore achieve the pressure losses target. Finally, the tube length per row decreases from 9.64 m to 7.45 m to keep the frontal exchanger area constant and, thus, to achieve the particle inlet velocity of 1 $\frac{mm}{s}$. A higher overall heat transfer coefficient could be obtained if higher particle inlet velocities are considered. For instance, a *U* value of 91.0 $\frac{W}{m^2K}$ and 115.2 $\frac{W}{m^2K}$ can be achieved for 2.5 $\frac{mm}{s}$ and 5 $\frac{mm}{s}$, respectively. The total heat exchange area decreases due to the higher *U*. The number of rows increases significantly, up to 145. The tube length row decreases, and so does also the total tube length. Then, the number of columns decreases to achieve a higher circulating velocity.

Table 14: *Design results for the COMPASsCO$_2$ HX at different $v_{p,in}$. Particle-side h_p being calculated with Bartsch's model.*

Parameter	Reference value	$v_{p,in} = 1\frac{mm}{s}$	$v_{p,in} = 2.5\frac{mm}{s}$	$v_{p,in} = 5\frac{mm}{s}$
Tube length per row [m]	9.64	7.45	3.34	1.81
Number of columns	271	350	312	288
Number of rows	20	51	92	145
Total external surface [m^2]	9897.9	25190	18175	14351
U [$\frac{W}{m^2K}$]	166.43	65.4	91.0	115.2

It is concluded that the COMPASsCO$_2$ design overestimates the overall transfer coefficient. Moreover, the implemented particle-side heat transfer coefficient model does not consider how an increasing number of rows penalizes such heat transfer coefficient on the particle side. However, the literature mentions this effect in [70, 74]. Therefore, the heat transfer coefficient could be even lower, and this may be due to the increasing penetrating resistance between the particles around

the tubes in the HX. It also has to be noted that the pressure losses calculation does not consider the pressure losses that happen in the 180º bends, which could be crucial for configurations with a huge number of rows. The effect of the number of rows on both the heat transfer coefficient and pressure losses will be evaluated in future work.

5.4 Heat exchanger design

Given the successful validation of the model and the satisfying results, the following step was the primary heat exchanger design. In particular, this heat exchanger is designed for two next-generation power generation systems: the first one is a Supercritical Recompression cycle running on pure sCO_2; the second one is a power system being investigated within the European-funded project SCARABEUS, and consists of a Transcritical Recompression Cycle running on a mixture of CO_2 and SO_2. The boundary conditions for each system are indicated in Tabs.[15] - [16] and, regarding the tube bank configuration, the same one from COMPASsCO_2 investigation has been adopted. As for the particle inlet velocity, a value of $v_p = 2.5\frac{mm}{s}$ is selected. Numerical results from the design have been resumed in Tabs. [17] - [18]. For more information of the technology, check the following references by the SCARABEUS project [75, 76].

Table 15: Supercritical recompression parameters summary.

Parameter	Value	Unit
Working fluid	sCO_2	-
Particles	CARBO ID50	-
Particle diameter, d_p	350	μm
Particles mass flow rate,$\dot{m}_p$	801	$\frac{kg}{s}$
Inlet particles temperature	800	°C
Outlet particles temperature	600	°C
Inlet WF.	550	°C
Outlet WF.	700	°C
Inlet WF. pressure	242.7	bar
Outlet WF. pressure	239.1	bar
WF. mass flow rate $\dot{m}_{WF}$	1059.3	$\frac{kg}{s}$
Tube diameter, D_{ext}	60.3	mm
S_v	77.7	mm
S_h	69.3	mm
Tube thickness, th_{tube}	5.22	mm
Material	Haynes 282 [73]	-
Particle inlet velocity, $v_{p,in}$	2.5	$\frac{mm}{s}$
Packed volume fraction	0.55	-

Table 16: Transcritical recompression parameters summary.

Parameter	Value	Unit
Working fluid	CO_2-SO_2 mix	-
Particles	CARBO ID50	-
Particle diameter, d_p	350	μm
Particles mass flow rate,$\dot{m}_p$	781.9	$\frac{kg}{s}$
Inlet particles temperature	800	°C
Outlet particles temperature	600	°C
Inlet WF.	499	°C
Outlet WF.	700	°C
Inlet WF. pressure	248.8	bar
Outlet WF. pressure	247.7	bar
WF. mass flow rate $\dot{m}_{WF}$	833.7	$\frac{kg}{s}$
Tube diameter, D_{ext}	60.3	mm
S_v	77.7	mm
S_h	69.3	mm
Tube thickness, th_{tube}	5.34	mm
Material	Haynes 282 [73]	-
Particle inlet velocity, $v_{p,in}$	2.5	$\frac{mm}{s}$
Packed volume fraction	0.55	-

Table 17: *Pure sCO_2 design.*

Parameter	Value	Unit
Overall *U*	91.0	$\frac{W}{m^2K}$
N. of rows	92	-
N. of columns	547	-
Tube length per row	4.66	m
Tot. width	37.9	m
Tot. height	7.1	m
Tot. external surface	44389	m^2
Tot. HX volume	1261.7	m^3

Table 18: *SCARABEUS mixture design.*

Parameter	Value	Unit
Overall *U*	88.9	$\frac{\mathrm{W}}{\mathrm{m^2K}}$
N. of rows	62	–
N. of columns	585	–
Tube length per row	4.25	m
Tot. width	40.5	m
Tot. height	4.8	m
Tot. external surface	29210.8	m^2
Tot. HX volume	830.3	m^3

As we can see from the comparative analysis presented in the two tables, the overall HTC (U) values for the two fluids are quite similar, with only a slight difference in favor of the SCARABEUS CO_2-SO_2 mixture. However, what is truly noteworthy is the significant reduction in volume (-34.2%) and total external surface area (-34.2%) achieved by the SCARABEUS mixture. This fascinating result implies that the same amount of heat exchange can be accomplished with smaller components, which has positive economic implications. Specifically, the use of less material in the design of the SCARABEUS mixture means lower costs of investment, which can be a considerable advantage. Moreover, the lower particle mass flow rate in the SCARABEUS mixture design means that there will be less material required, leading to additional cost savings. This, in turn, can bring further benefits to the LCOE (Levelized Cost of Electricity) of the entire power plant, making it more cost-effective in the long run. To achieve goals with lower costs, it is crucial to develop new working fluid mixtures and explore innovative technologies. This study highlights the significance of these pursuits.

6 Conclusions and future developments

This paper has provided a comprehensive analysis of the solar subsystem of next-generation CSP power plant with a focus on the heat exchanger and the solar receiver modelling. It has been found that falling particle receivers are the most promising technology for achieving high temperatures in CSP power plants due to their ability to withstand temperatures higher than 800°C, considering also the commercial partner suggestion.

The three-receiver tower configuration has been found to be the most efficient design, requiring only 9000 heliostats, achieving an overall efficiency of 47.78% and a power input of 638.17 MW. The non-uniform irradiance analysis that was conducted on a three-receiver tower receiver enabled the achievement of a solar field design that was both efficient and effective. Furthermore, this paper has demonstrated that particles can achieve an outlet receiver temperature of 800°C with a receiver efficiency of 81.5%, which is a crucial finding in the development of next-generation CSP power plants.

The literature review conducted on particle-to-sCO_2 heat exchangers has identified the shell and tube moving packed bed configuration as the most promising technology to be coupled with a falling particle receiver. In this regard, the assessment of the heat transfer coefficient on the particle side is a novel contribution of the present paper.

The heat exchanger modelling and the HTC of the particles have been explained in detail, and the validation of the heat exchanger against the COMPASsCO_2S heat exchanger model has shown that the overall heat transfer coefficient U value is much lower when the HTC model is included (U=166.43 $\frac{\mathrm{W}}{\mathrm{m^2K}}$ from COMPASsCO_2 deliverable [72] against 64.5 $\frac{\mathrm{W}}{\mathrm{m^2K}}$) [see Tab.[14]). Additionally, this paper has shown that the U value depends on the particle inlet velocity, with a higher velocity resulting in a higher heat transfer coefficient which is consistent with previous studies.

An analysis on two mixtures, pure sCO_2 and a SCARABEUS fluid mixture of CO_2 and SO_2, have been conducted. The analysis of two fluid mixtures reveals that their overall heat transfer coefficients (HTC) are quite similar, with a slight advantage for the SCARABEUS CO_2-SO_2 mixture. However, what is more significant is that the SCARABEUS mixture has achieved a substantial reduction in volume and total external surface area. This means that the same heat exchange can be achieved with smaller components, resulting in lower material costs and investment.

Overall, the reduction in volume and surface area achieved by the SCARABEUS CO_2-SO_2 mixture is a significant development, which has practical and economic implications. These findings highlight the importance of investing in innovative technologies that can improve the efficiency and sustainability of power generation systems.

In conclusion, three clear topics can be identified as future developments of the present work: the development of two specific models for a particle-based TES and a centrifugal receiver, and a general enhancement of thermal correlations employed and the characterization of the particles considered. Firstly, as highlighted in the previous sections, implementing a TES system is essential for storing energy and making thermal energy available when needed, even when solar irradiation is not available [49]. In this regard, a specific model would allow to provide a closer insight into this equipment, assessing its contribution to the techno-economic performance of the CSP plant. Secondly, the identification of the optimum solar particle receiver is a crucial aspect in the optimization of next generation CSP plants. For sake of simplicity, the preliminary study presented in this paper considered a free falling particle receiver instead of a centrifugal one, due to the lack of several information needed to assess a detailed model of the latter. Bearing this in mind, a natural development of this research work is the assessment of a centrifugal receiver, also by means of specific CFD studies to estimate in detail the heat transfer correlations in this component. Finally, a series of updated information could be considered in future works, i.e. enhanced thermal correlations and characterization of particles that may be found in the framework of other research projects such as COMPASsCO_2SsCO_2. In this regard, it is crucial to find new granular materials that can prevent particle ageing and loss of their optical properties due to exposure to high temperatures. The new models should also incorporate the variable heat transfer coefficient and the study on the variations in the heat transfer coefficient based on the number of rows, to take into account the heterogeneous heat transfer between particles and working fluid.

References

[1] R.P. Merchán, M.J. Santos, A. Medina, and A. Calvo Hernández. High temperature central tower plants for concentrated solar power: 2021 overview. *Renewable and Sustainable Energy Reviews*, 155:111828, 2022. ISSN 1364-0321. doi: https://doi.org/10.1016/j.rser.2021.111828. URL https://www.sciencedirect.com/science/article/pii/S1364032121010923.

[2] Clifford K Ho. A review of high-temperature particle receivers for concentrating solar power. *Applied Thermal Engineering*, 109:958–969, 2016.

[3] Clifford K. Ho, Matthew Carlson, Kevin J. Albrecht, Zhiwen Ma, Sheldon Jeter, and Clayton M. Nguyen. Evaluation of alternative designs for a high temperature particle-to-sco 2 heat exchanger. *Journal of Solar Energy Engineering, Transactions of the ASME*, 141, 4 2019. ISSN 15288986. doi: 10.1115/1.4042225.

[4] Zhiwen Ma, Xingchao Wang, Patrick Davenport, Jeffrey Gifford, and Janna Martinek. Economic analysis of a novel thermal energy storage system using solid particles for grid electricity storage: Preprint. URL https://www.nrel.gov/docs/fy21osti/79014.pdf.

[5] Zhiwen Ma, Xingchao Wang, Patrick Davenport, Jeffery Gifford, and Janna Martinek. Preliminary component design and cost estimation of a novel electric-thermal energy storage system using solid particles. *Journal of Solar Energy Engineering, Transactions of the ASME*, 144, 6 2022. ISSN 15288986. doi: 10.1115/1.4053256.

[6] International Energy Agency (IEA). World energy outlook 2020. 2020.

[7] Luis F. González-Portillo, Kevin Albrecht, and Clifford K. Ho. Techno-economic optimization of csp plants with free-falling particle receivers. *Entropy*, 23:1–24, 1 2021. ISSN 10994300. doi: 10.3390/e23010076.

[8] Abdelrahman El-Leathy, Hany Al-Ansary, Syed Noman Danish, Anas Alsuhaibani, and Abdulelah Alswaiyd. An investigation of the optimum solar flux distribution on a large-scale particle heating receiver. *Frontiers in Energy Research*, 10, 2 2022. ISSN 2296598X. doi: 10.3389/fenrg.2022.823448.

[9] Clifford K. Ho. Advances in central receivers for concentrating solar applications. *Solar Energy*, 218:415–428, 2017.

[10] Bekir Yilbas and Sameer Shuja. A solar volumetric receiver: Influence of absorbing cells configuration on device thermal performance. *International Journal of Thermophysics*, 38:1, 11 2016. doi: 10.1007/s10765-016-2132-3.

[11] M. Chinappi, G. M. Giusti, L. Sterbini, S. Carmignani, and G. Tanda. Thermal characterization of a novel high-temperature multi-tube receiver. *Solar Energy*, 97:168–177, 2013.

[12] Kaijun Jiang, Xiaoze Du, Qiang Zhang, Yanqiang Kong, Chao Xu, and Xing Ju. Review on gas-solid fluidized bed particle solar receivers applied in concentrated solar applications: Materials, configurations and methodologies. *Renewable and Sustainable Energy Reviews*, 150:111479, 2021.

[13] Ambra Giovannelli. State of the art on small-scale concentrated solar power plants. *Energy Procedia*, 82:607–614, 2015.

[14] Steven Hegedus and Antonio Luque. *Handbook of photovoltaic science and engineering*. John Wiley & Sons, 2011.

[15] Ugo Pelay, Lingai Luo, Yilin Fan, Driss Stitou, and Mark Rood. Thermal energy storage systems for concentrated solar power plants. *Renewable and Sustainable Energy Reviews*, 79:82–100, 2017.

[16] David Kearney, Ulf Herrmann, Paul Nava, B Kelly, Rod Mahoney, James Pacheco, Robert Cable, N Potrovitza, Daniel Blake, and Henry Price. Assessment of a molten salt heat transfer fluid in a parabolic trough solar field. *J. Sol. Energy Eng.*, 125(2):170–176, 2003.

[17] Madjid Sarvghad, Teng C. Ong, Stuart Bell, Raihan Rumman, Salar Delkasar Maher, Jack W. Woodcock, Geoffrey Will, Gunther Andersson, David A. Lewis, and Theodore A. Steinberg. On the compatibility of liquid sodium as heat transfer fluid for advanced concentrated solar thermal energy systems. *Solar Energy Materials and Solar Cells*, 246: 111897, 2022. ISSN 0927-0248. doi: https://doi.org/10.1016/j.solmat.2022.111897. URL https://www.sciencedirect.com/science/article/pii/S0927024822003178.

[18] Nicholas Boerema, Graham Morrison, Robert Taylor, and Gary Rosengarten. Liquid sodium versus hitec as a heat transfer fluid in solar thermal central receiver systems. *Solar Energy*, 86(9):2293–2305, 2012. ISSN 0038-092X. doi: https://doi.org/10.1016/j.solener.2012.05.001. URL https://www.sciencedirect.com/science/article/pii/S0038092X12001703.

[19] J.R. Richard, R. Delbourgo, and P. Laffitte. Spontaneous ignition and combustion of sodium droplets in various oxidizing atmospheres at atmospheric pressure. *Symposium (International) on Combustion*, 12(1):39–48, 1969. ISSN 0082-0784. doi: https://doi.org/10.1016/S0082-0784(69)80390-5. URL https://www.sciencedirect.com/science/article/pii/S0082078469803905.

[20] Belén Zalba, José M Marın, Luisa F. Cabeza, and Harald Mehling. Review on thermal energy storage with phase change: materials, heat transfer analysis and applications. *Applied Thermal Engineering*, 23(3):251–283, 2003. ISSN 1359-4311. doi: https://doi.org/10.1016/S1359-4311(02)00192-8. URL https://www.sciencedirect.com/science/article/pii/S1359431102001928.

[21] Emiliano Casati and Aldo Steinfeld. Direct absorption of concentrated solar radiation by glass above 1000 °c. page 200010, 2019. doi: 10.1063/1.5117725. URL http://aip.scitation.org/doi/abs/10.1063/1.5117725.

[22] Qiang Yu, Peng Fu, Yihui Yang, Jiafei Qiao, Zhifeng Wang, and Qiangqiang Zhang. Modeling and parametric study of molten salt receiver of concentrating solar power tower plant. *Energy*, 200:117505, 2020. ISSN 0360-5442. doi: https://doi.org/10.1016/j.energy.2020.117505. URL https://www.sciencedirect.com/science/article/pii/S0360544220306125.

[23] Clifford K Ho, Joshua M Christian, Julius Yellowhair, Kenneth Armijo, William J Kolb, Sheldon Jeter, Matthew Golob, and Clayton Nguyen. Performance evaluation of a high-temperature falling particle receiver, 2016.

[24] Yifan Liu, Jiajia Cai, Yuanyuan Hu, Sheng Yu, and Yuan Wang. Investigation of the porous barrier effect on particle residence time in a solar particle receiver. *Applied Thermal Engineering*, 169:114976, 2020. doi: 10.1016/j.applthermaleng.2020.114976.

[25] Chunyan Lou, Xing Liu, Jing Ma, Lei Wang, and Zhifeng Wang. Numerical simulation on porous barriers in solar particle receiver. *Energy Procedia*, 158:3500–3505, 2019. doi: 10.1016/j.egypro.2019.01.843.

[26] F Reche, E Bartolom'e, A Coronas, and A Oliva. Thermal performance of a pilot-scale indirect particle receiver for high-temperature solar thermal applications. *Applied Thermal Engineering*, 164:114491, 2020.

[27] C Sole, A Oliva, F Reche, E Bartolome, and A Coronas. Experimental analysis of a fluidized bed as a heat transfer fluid in a high-temperature solar receiver. *Renewable Energy*, 150: 625–637, 2020.

[28] F Reche, E Bartolomé, A Coronas, and A Oliva. Design and optimization of an indirect particle receiver for high-temperature solar thermal applications. *Solar Energy*, 215:553–564, 2021.

[29] Kaijun Jiang, Xiaoze Du, Qiang Zhang, Yanqiang Kong, Chao Xu, and Xing Ju. Review on gas-solid fluidized bed particle solar receivers applied in concentrated solar applications: Materials, configurations and methodologies. *Renewable and Sustainable Energy Reviews*, 150:111479, 2021. ISSN 1364-0321. doi: https://doi.org/10.1016/j.rser.2021.111479. URL https://www.sciencedirect.com/science/article/pii/S1364032121007607.

[30] R. Morgan, H. Huang, and R. Boehm. Thermal performance of a staggered array of tubes for use in an indirectly heated particle receiver. *Solar Energy*, 119:489–500, 2015.

[31] Miriam Ebert, Lars Amsbeck, Reiner Buck, Jens Rheinländer, Bärbel Schlögl-Knothe, Stefan Schmitz, Marcel Sibum, Hannes Stadler, and Ralf Uhlig. First on-sun tests of a centrifugal particle receiver system, 2018.

[32] Miriam Ebert, Lars Amsbeck, Jens Rheinländer, Bärbel Schlögl-Knothe, Stefan Schmitz, Marcel Sibum, Ralf Uhlig, and Reiner Buck. Operational experience of a centrifugal particle receiver prototype. *AIP Conference Proceedings*, 2126, 7 2019. ISSN 15517616. doi: 10.1063/1.5117530.

[33] W. Wu, D. Trebing, L. Amsbeck, R. Buck, and R. Pitz-Paal. Prototype testing of a centrifugal particle receiver for high-temperature concentrating solar applications. *Journal of Solar Energy Engineering, Transactions of the ASME*, 137(4), 2015. doi: 10.1115/1.4030657. URL https://www.scopus.com/inward/record.uri?eid=2-s2.0-84934969559&doi=10.1115%2f1.4030657&partnerID=40&md5=e40beea54113a913b1c56302428b0301. cited By 62.

[34] W. Wu, L. Amsbeck, R. Buck, R. Uhlig, and R. Ritz-Paal. Proof of concept test of a centrifugal particle receiver. volume 49, pages 560–568, 2014. doi: 10.1016/j.egypro.2014.03.060. URL https://www.scopus.com/inward/record.uri?eid=2-s2.0-84902270529&doi=10.101%2fj.egypro.2014.03.060&partnerID=40&md5=3838b0cc00b8ed82e43bfe39f596a50b. cited By 57.

[35] G3p3 techno-economic analysis of up-scaled centrec receiver modelling parameters and results 2 document properties title g3p3 techno-economic analysis of up-scaled centrec receiver.

[36] Wei Wu. A centrifugal particle receiver for high-temperature solar applications. - chap. 4: Numerical receiver model, 2014. URL http://ebookcentral.proquest.com/lib/uses/detail.action?docID=5231176.

[37] Serdar Hicdurmaz, Evan F. Johnson, Johannes Grobbel, Lars Amsbeck, Reiner Buck, and Bernhard Hoffschmidt. Numerical heat transfer modelling of a centrifugal solar particle receiver. volume 2445. American Institute of Physics Inc., 5 2022. ISBN 9780735441958. doi: 10.1063/5.0086375.

[38] Johannes Grobbel. Modeling solar particle receivers with the discrete element method modellierung von solaren partikelreceivern mit der diskreten elemente methode.

[39] Andrew S Oles. Title of document: Modeling of falling-particle solar receivers for hydrogen production and thermochemical energy storage, 2014.

[40] James E Pacheco and Steven K Showalter. Particle receiver progress at sandia national laboratories. *Solar Energy*, 32(5):557–567, 1984.

[41] P K Falcone, J E Noring, and J M Hruby. Sand ia repor t sand85-8208 • unlimited re as : Uc- 2 assessment of a solid particle · receiver for a high temperature solar central receiver system sf 2900-q(6-82

[42] Wei Wang, Yong Shuai, Bachirou Guene Lougou, and Boshu Jiang. Thermal performance analysis of free-falling solar particle receiver and heat transfer modelling of multiple particles. *Applied Thermal Engineering*, 187:116567, 3 2021. ISSN 1359-4311. doi: 10.1016/J.APPLTHERMALENG.2021.116567.

[43] Clifford K. Ho, Joshua M. Christian, David Romano, Julius Yellowhair, Nathan Siegel, Laura Savoldi, and Roberto Zanino. Characterization of particle flow in a free-falling solar particle receiver. *Journal of Solar Energy Engineering, Transactions of the ASME*, 139, 4 2017. ISSN 15288986. doi: 10.1115/1.4035258/392605. URL https://asmedigitalcollection.asme.org/solarenergyengineering/article/139/2/021011/392605/Characterization-of-Particle-Flow-in-a-Free.

[44] Andrew S. Oles and Gregory S. Jackson. Modeling of a concentrated-solar, falling-particle receiver for ceria reduction. *Solar Energy*, 122:126–147, 12 2015. ISSN 0038-092X. doi: 10.1016/J.SOLENER.2015.08.009.

[45] Brantley Mills and Clifford K. Ho. Annualized thermal performance of intermediate-scale falling particle receivers. volume 2033. American Institute of Physics Inc., 11 2018. ISBN 9780735417571. doi: 10.1063/1.5067062.

[46] C. Ho, J. Christian, D. Gill, A. Moya, S. Jeter, S. Abdel-Khalik, D. Sadowski, N. Siegel, H. Al-Ansary, L. Amsbeck, B. Gobereit, and R. Buck. Technology advancements for next generation falling particle receivers. *Energy Procedia*, 49:398–407, 2014. ISSN 1876-6102. doi: https://doi.org/10.1016/j.egypro.2014.03.043. URL https://www.sciencedirect.com/science/article/pii/S1876610214004974. Proceedings of the SolarPACES 2013 International Conference.

[47] Giampaolo Manzolini, Gaia Lucca, Marco Binotti, and Giovanni Lozza. A two-step procedure for the selection of innovative high temperature heat transfer fluids in solar tower power plants. *Renewable Energy*, 177:807–822, 2021. ISSN 0960-1481. doi: https://doi.org/10.1016/j.renene.2021.05.153. URL https://www.sciencedirect.com/science/article/pii/S0960148121008429.

[48] Zhiwen Ma, Patrick Davenport, and Ruichong Zhang. Design analysis of a particle-based thermal energy storage system for concentrating solar power or grid energy storage. *Journal of Energy Storage*, 29:101382, 2020.

[49] Anabel Palacios, Alejandro Calderón, Camila Barreneche, Joan Bertomeu, Mercè Segarra, and A. Inés Fernández. Study on solar absorptance and thermal stability of solid particles materials used as tes at high temperature on different aging stages for csp applications. *Solar Energy Materials and Solar Cells*, 201:110088, 2019. ISSN 0927-0248. doi: https://doi.org/10.1016/j.solmat.2019.110088. URL https://www.sciencedirect.com/science/article/pii/S0927024819304179.

[50] *Parametric Analysis of Particle CSP System Performance and Cost to Intrinsic Particle Properties and Operating Conditions*, volume ASME 2019 13th International Conference on Energy Sustainability of *Energy Sustainability*, 07 2019. doi: 10.1115/ES2019-3893. URL https://doi.org/10.1115/ES2019-3893. V001T03A006.

[51] Brantley Mills, Reid Shaeffer, Clifford K Ho, and Lindsey Yue. Modeling the thermal performance of falling particle receivers subject to external wind 1 authors: Sand2019-8101c.

[52] Luis F. González-Portillo, Rubén Abbas, Kevin Albrecht, and Clifford Ho. Analysis of optical properties in particle curtains. *Solar Energy*, 213:211–224, 2021. ISSN 0038-092X. doi: https://doi.org/10.1016/j.solener.2020.11.012. URL https://www.sciencedirect.com/science/article/pii/S0038092X20311609.

[53] Brantley H. Mills, Clifford K. Ho, Nathaniel R. Schroeder, Reid Shaeffer, Hendrik F. Laubscher, and Kevin J. Albrecht. Design evaluation of a next-generation high-temperature particle receiver for concentrating solar thermal applications, 3 2022. ISSN 19961073.

[54] Luis F. González-Portillo, Víctor Soria-Alcaide, Kevin Albrecht, Clifford K. Ho, and Brantley Mills. Benchmark and analysis of a particle receiver 1d model. *Solar Energy*, 255:301–313, 2023. ISSN 0038-092X. doi: https://doi.org/10.1016/j.solener.2023.03.046. URL https://www.sciencedirect.com/science/article/pii/S0038092X23002062.

[55] Marco Binotti, Marco Astolfi, Stefano Campanari, Giampaolo Manzolini, and Paolo Silva. Preliminary assessment of sco2 cycles for power generation in csp solar tower plants. *Applied energy*, 204:1007–1017, 2017.

[56] Csp summit2019 snl ho particlehx.

[57] Kevin J. Albrecht and Clifford K. Ho. Heat transfer models of moving packed-bed particle-to-sco2 heat exchangers. *Journal of Solar Energy Engineering, Transactions of the ASME*, 141, 6 2019. ISSN 15288986. doi: 10.1115/1.4041546.

[58] Zhiwen Ma and Janna Martinek. Analysis of a Fluidized-Bed Particle/Supercritical-CO2 Heat Exchanger in a Concentrating Solar Power System. *Journal of Solar Energy Engineering*, 143 (3), 10 2020. ISSN 0199-6231. doi: 10.1115/1.4048548. URL https://doi.org/10.1115/1.4048548. 031010.

[59] Congcong Wu, Haitao Yang, Xiaohei He, Chaoquan Hu, Le Yang, and Hongtao Li. Principle, development, application design and prospect of fluidized bed heat exchange technology: Comprehensive review. *Renewable and Sustainable Energy Reviews*, 157:112023, 2022.

[60] J.S.M. Botterill and A.O.O. Denloye. A theoretical model of heat transfer to a packed or quiescent fluidized bed. *Chemical Engineering Science*, 33(4):509–515, 1978. ISSN 0009-2509. doi: https://doi.org/10.1016/0009-2509(78)80011-6. URL https://www.sciencedirect.com/science/article/pii/0009250978800116.

[61] Wenchao Fang, Sheng Chen, Jingying Xu, and Kuo Zeng. Predicting heat transfer coefficient of a shell-and-plate, moving packed-bed particle-to-sco2 heat exchanger for concentrating solar power. *Energy*, 217:119389, 2021.

[62] Nicolas A DeLovato, Kevin Albrecht, and Clifford Ho. Thermomechanical modeling of counterflow packed-bed particle-to-sco2 heat exchangers. In *AIP Conference Proceedings*, volume 2445, page 030004. AIP Publishing LLC, 2022.

[63] Kevin J. Albrecht and Clifford K. Ho. Design and operating considerations for a shell-and-plate, moving packed-bed, particle-to-sco2 heat exchanger. *Solar Energy*, 178:331–340, 2019. ISSN 0038-092X. doi: https://doi.org/10.1016/j.solener.2018.11.065. URL https://www.sciencedirect.com/science/article/pii/S0038092X18311721.

[64] Ammar Ali Abd, Mohammed Qasim Kareem, and Samah Zaki Naji. Performance analysis of shell and tube heat exchanger: Parametric study. *Case Studies in Thermal Engineering*, 12:563–568, 2018. ISSN 2214-157X. doi: https://doi.org/10.1016/j.csite.2018.07.009. URL https://www.sciencedirect.com/science/article/pii/S2214157X17303416.

[65] Ammar Ali Abd and Samah Zaki Naji. Analysis study of shell and tube heat exchanger for clough company with reselect different parameters to improve the design. *Case studies in thermal engineering*, 10:455–467, 2017.

[66] Yen Chean Soo Too, Jin-Soo Kim, Sahan Trushad Wickramasooriya Kuruneru, Ryan Stiff, and Adrian Dawson. Development of a staged particle heat exchanger for particle thermal energy storage systems. *Solar Energy*, 220:111–118, 2021. ISSN 0038-092X. doi: https://doi.org/10.1016/j.solener.2021.03.014. URL https://www.sciencedirect.com/science/article/pii/S0038092X21002000.

[67] Torsten Baumann and Stefan Zunft. Development and performance assessment of a moving bed heat exchanger for solar central receiver power plants. *Energy Procedia*, 69:748–757, 2015.

[68] Philipp Bartsch Aus Würzburg and Aus Würzbslleeecurg. Von der fakultät energie-, verfahrens-und biotechnik der entwicklung neuer modelle zur beschreibung von schüttgutströmungen in wanderbettwärmeübertragern, 2020.

[69] Julian D. Hertel and Stefan Zunft. Experimental validation of a continuum model for local heat transfer in shell-and-tube moving-bed heat exchangers. *Applied Thermal Engineering*, 206: 118092, 2022. ISSN 1359-4311. doi: https://doi.org/10.1016/j.applthermaleng.2022.118092. URL https://www.sciencedirect.com/science/article/pii/S1359431122000576.

[70] Jörg Niegsch. *Schüttgutbewegung und Wärmeübergang im Wanderbett*. Shaker, 1993.

[71] J A M Kuipers, W Prins, and W P M Van Swaaij. Numerical calculation of wall-to-bed heat-transfer coefficients in gas-fluidized beds.

[72] Lukas Heller Dlr, Maxime Rouzes, John Cockerill, Hicham Barbri Dlr, Daniel Benitez, Dlr Reiner, and Buck Dlr. Compassco2-components' and materials' performance for advanced solar supercritical co2 power plants deliverable 1.2 "process parameters of solar particle cycle".

[73] Abdullah Ali Mohammed Ba Gunaid. *Development of a Preliminary Design and a One-Dimensional Model for a Direct Contact Heat Exchanger*. PhD thesis, Georgia Institute of Technology, 2022.

[74] J Niegsch, D Köneke, and P-M Weinspach. Heat transfer and flow of bulk solids in a moving bed. *Chemical Engineering and Processing: Process Intensification*, 33(2):73–89, 1994.

[75] Pablo Rodríguez-deArriba, Francesco Crespi, David Sánchez, Antonio Muñoz, and Tomás Sánchez. The potential of transcritical cycles based on co2 mixtures: An exergy-based analysis. *Renewable Energy*, 199:1606–1628, 2022. ISSN 0960-1481. doi: https://doi.org/10.1016/j.renene.2022.09.041. URL https://www.sciencedirect.com/science/article/pii/S096014812201391X.

[76] F. Crespi, P. Rodríguez de Arriba, D. Sánchez, A. Ayub, G. Di Marcoberardino, C.M. Invernizzi, G.S. Martínez, P. Iora, D. Di Bona, M. Binotti, and G. Manzolini. Thermal efficiency gains enabled by using co2 mixtures in supercritical power cycles. *Energy*, 238: 121899, 2022. ISSN 0360-5442. doi: https://doi.org/10.1016/j.energy.2021.121899. URL https://www.sciencedirect.com/science/article/pii/S0360544221021472.

Acknowledgements

The ISOP project has received funding from the European Union's Marie Skłodowska-Curie Actions under grant agreement Nº101073266. The Spanish Ministry of Universities is gratefully acknowledged for sponsoring the contract of Pablo Rodríguez de Arriba via FPU (Formación de Profesorado Universitario). Grant reference FPU21/04892.